The Pristine survey - XIX: Cu and Zn abundances in metal-poor giants

E. Caffau, L. Lombardo, L. Mashonkina, T. Sitnova, P. Bonifacio, A. M. Matas Pinto, G. Kordopatis, F. Sestito, D. Aguado, S. Salvadori, et al.

Monthly Notices of the ROYAL ASTRONOMICAL SOCIETY

MNRAS **518,** 3796–3812 (2023) https://doi.org/10.1093/mnras/stac3372
Advance Access publication 2022 November 21

The Pristine survey – XIX. Cu and Zn abundances in metal-poor giants

E. Caffau,[1]★ L. Lombardo,[1] L. Mashonkina,[2] T. Sitnova,[2] P. Bonifacio,[1] A. M. Matas Pinto,[1] G. Kordopatis,[3] F. Sestito,[4] D. Aguado,[5,6] S. Salvadori,[5,6] M. Spite,[1] P. François,[1,7] L. Sbordone,[8] A. Mucciarelli,[9,10] N. Martin,[11] E. Fernández-Alvar[12,13] and J. I. González Hernández[12,13]

[1]*GEPI, Observatoire de Paris, Université PSL, CNRS, Place Jules Janssen, F-92190 Meudon, France*
[2]*Institute of Astronomy, Russian Academy of Sciences, Pyatnitskaya st 48, 119017 Moscow, Russia*
[3]*Université Côte d'Azur, Observatoire de la Côte d'Azur, CNRS, Laboratoire Lagrange, Bd de l'Observatoire CS 34229 - F 06304 Nice Cedex 4, France*
[4]*Department of Physics and Astronomy, University of Victoria, Victoria, BC V8P 5C2, Canada*
[5]*Dipartimento di Fisica e Astronomia, Università degli Studi di Firenze, via G. Sansone 1, I-50019 Sesto Fiorentino, Italy*
[6]*INAF – Osservatorio Astrofisico di Arcetri, Largo E. Fermi 5, I-50125 Firenze, Italy*
[7]*GEPI, Observatoire de Paris, Université PSL, CNRS, 77 Av. Denfert-Rochereau, F-75014 Paris, France*
[8]*European Southern Observatory, Alonso de Cordova 3107, Vitacura, Santiago, Chile*
[9]*Dipartimento di Fisica e Astronomia 'Augusto Righi', Alma Mater Studiorum, Università di Bologna, Via Gobetti 93/2, I-40129 Bologna, Italy*
[10]*INAF – Osservatorio di Astrofisica e Scienza dello Spazio di Bologna, Via Gobetti 93/3, I-40129 Bologna, Italy*
[11]*Observatoire astronomique de Strasbourg, Université de Strasbourg, CNRS, UMR 7550, F-67000, Strasbourg, France*
[12]*Instituto de Astrofísica de Canarias, E-38200 La Laguna, Tenerife, Spain*
[13]*Dept. Astrofísica, Universidad de La Laguna, E-38206 La Laguna, Tenerife, Spain*

Accepted 2022 November 9. Received 2022 November 9; in original form 2022 August 29

ABSTRACT

Metal-poor stars formed from a gas enriched by the ejecta of the explosion of one/few generations of first massive stars. With the Pristine photometry combined with the *Gaia* data, we selected a sample of bright giants metal-poor candidates to be observed at high resolution. Of the 43 stars observed, 36 were confirmed to be metal-poor, supporting the high success-rate of Pristine in selecting metal-poor stars. We centred the investigation on Cu and Zn, which are elements usually neglected, also because they are the 'killing elements' for identifying the Pair Instability Supernovae (PISN) descendants, the explosion of very massive first stars. We derived detailed chemical abundances of 22 species of 18 elements for 36 giant stars. The study of the kinematics of the stars in the sample revealed the presence of metal-poor stars on disc-like orbits (17 per cent of the sample) and even on thin disc orbits (8 per cent of the sample). Four stars are members of the Gaia–Sausage–Enceladus, one star is also likely a member of it. Three stars in the sample (TYC 1118−595−1, TYC 2207−992−1, and TYC 1194−507−1) show a chemical pattern compatible with the one theoretically derived for the PISN descendants, i.e. stars formed out from a gaseous environment enriched by PISN (>50 per cent level) and subsequent generations of normal stars evolving as core-collapse SNe.

Key words: stars: abundances – stars: evolution – Galaxy: abundances – Galaxy: evolution.

1 INTRODUCTION

The formation of elements up to iron can take place in the stellar interior through exothermal nuclear reactions, while elements heavier than Fe need energy to be formed. The elements Cu and Zn (neighbours in the periodic table with 29 and 30 protons, respectively) belong to the iron peak and have to be formed via exothermal nuclear reactions. Both Cu and Zn are elusive in our understanding of their chemical evolution and their production sites.

Bisterzo et al. (2004) suggested several sites for the copper production: (i) explosive nucleosynthesis in Type II supernovae and (ii) in Type Ia supernovae, (iii) through the weak s-process (neutron-capture process followed by β decay) in massive stars, (iv) through the main s-process in asymptotic giant branch (AGB) stars, and (v) through the weak sr-process in the C-burning shell of massive stars. In massive stars, the s-process is possible thanks to the ^{22}Ne $(\alpha, n)^{25}$ Mg reaction, which provides neutrons. This is the main production channel of Cu, with a minor contribution from explosive nucleosynthesis (Bisterzo et al. 2005). According to Pignatari et al. (2010), the main production sites of Cu within the Milky Way are massive stars. This occurs through the weak s-process in the stellar core during the phase of He burning, and in the C-burning shell. On the other hand, copper and zinc are not expected to be efficiently produced by the s-process during the AGB phase. This view is supported by Kratz et al. (2008), who conclude that the main r-process is not an efficient way to produce Cu. Romano & Matteucci (2007) agree that the weak s-process is the main Cu contributor, but they state that, at extremely low metallicity, Cu is essentially produced by nucleosynthesis in massive stars explosions.

The efficiency in the Cu production via the weak s-process is dependent on the stellar metallicity, in particular, we observe that the [Cu/Fe] ratio decreases with decreasing metallicity (Bisterzo et al. 2005; Romano & Matteucci 2007). This strong dependence

★ E-mail: elisabetta.caffau@obspm.fr

on metallicity of Cu production results from the use of 1D models and the assumption of local thermodynamic equilibrium (LTE) for investigating this element (see e.g. Mishenina et al. 2002; Bihain et al. 2004). Taking into account the departures from LTE (NLTE) in the investigation on Cu I lines, the decrease in [Cu/Fe] with decreasing metallicity is much reduced (see e.g. Yan, Shi & Zhao 2015; Shi et al. 2018) or cancelled (Andrievsky et al. 2018). Roederer & Barklem (2018) investigated neutral and single ionised Cu lines and highlighted a much smoother decrease of [Cu/Fe] with metallicity when using the abundances derived from Cu II lines, which form closer to LTE condition than neutral lines. The chemical evolution model by Romano & Matteucci (2007) is able to well reproduce the observations of Shi et al. (2018) by taking into account explosive nucleosynthesis.

The situation for Zn production is more complicated than for Cu, for an overview see e.g. Hirai et al. (2018). Several Zn isotopes are stable (^{64}Zn, ^{66}Zn, ^{67}Zn, ^{68}Zn, ^{70}Zn) and several astronomical sites and channels have been proposed to produce them. The Solar system per cent isotopic fractions of these five isotopes are: 49.17, 27.73, 4.04, 18.45, 0.61 (Lodders 2019). ^{64}Zn and ^{66}Zn can be produced in massive stars via α-rich freeze-out in ν winds (Pignatari et al. 2010). The heaviest Zn isotopes are produced in the weak s-process (Bisterzo et al. 2005). Other sources of Zn in the Galactic evolution are: hypernovae, electron-capture supernovae, and supernovae (Hirai et al. 2018). Romano et al. (2010) compared several models of chemical evolution of Zn to Galactic observed measurements, finding a reasonable agreement, but no model could really reproduce completely, in a quantitative way, the [Zn/Fe] versus [Fe/H] results.

Zn has been the object of several Galactic investigations in the past decades (see e.g. Duffau et al. 2017). So far the observations have not been able to confirm which are the favoured channels (if any) for the Cu and Zn production. The intermediate metallicity range from $-2.5 \leq$ [Fe/H] ≤ -1.5 is not usually the most investigated. In fact, several investigations on Zn at higher metallicity have been published (see e.g. Mishenina et al. 2016) and also large samples of stars have been analysed (see e.g. Delgado Mena et al. 2017) in a way to provide also a large statistic. The metallicity range $-3.0 <$ [Fe/H] < -1.5 can count usually only on small samples (see e.g. Mishenina et al. 2002) and the same holds true for Cu, for which also at metal-rich regime the statistics are limited.

But there is something more. Cu and Zn are two of the key elements (another one being N) to select the stars formed from a gas predominantly enriched by zero-metallicity Pair Instability Supernovae (PISN; see Salvadori et al. 2019). Among the first generation (Pop III) stars, the massive ones with $140\,M_\odot < M < 260\,M_\odot$ are expected to conclude their lives as PISN, an energetic explosion that leaves no remnant (Woosley, Heger & Weaver 2002). In this way, all the stellar mass is released in the gas, with 50 per cent in the form of heavy elements. The frequency of PISN is unknown but it is expected to be very small (see e.g. de Bennassuti et al. 2017; Rossi, Salvadori & Skúladóttir 2021) and even their existence is still debated. A way to verify their existence and eventually determine their frequency is to search for their descendants. The descendent of PISN explosions are expected to be metal-poor stars, in a broad range ($-4 <$ [Fe/H] < -1) with a peak at [Fe/H] ~ -1.8 (see Salvadori et al. 2019). As stated by Salvadori et al. (2019), from a chemical point of view the direct PISN descendent, meaning the stellar generations formed from a gas enriched by a PISN explosion, are characterized by some key elements underabundant with respect to Fe: N, F, Na, Sc, V, Cu, and Zn. However, when accounting for the chemical contribution of normal stars exploding as type II SNe, one obtains that only the killing element ratios [N/Fe], [Cu/Fe], and [Zn/Fe] preserve a sub-solar value in PISNe-dominated environment (>50 per cent of metals; Salvadori et al. 2019). Among these elements, the ones showing the most extreme paucity are N, F, Cu, and Zn. One has to take into account the fact that the PISN ejecta can be diluted in a gas enriched by Type II supernovae, so that the signature of low [Cu/Fe] and [Zn/Fe] ratios in the stellar atmosphere is also diminished. The ratios do not have a preferred value, in principle that can be as tiny as to be detectable. In our analysis, we put a cut at a contribution by PISN of 50 per cent.

One of the reasons why Cu and Zn are not often investigated is also the relatively small number of atomic lines in the stellar spectra. Few lines are available in the optical wavelength range to investigate these two elements. Four Cu I lines (510.5, 521.8, 570.0, and 578.2 nm) allow to derive the Cu abundance. These lines are not strong and they vanish in the metal-poor regime. Two Zn I lines at 472.2 and 481.0 nm are usually investigated to derive the Zn abundance. For extremely metal-poor ([Fe/H]<-3.5) stars, the Zn and Cu lines are very rarely detectable. Some Cu and Zn abundances are provided in the literature also in the extremely metal-poor regime ([Fe/H]<-3.5), in the case of Zn mainly for Zn-rich stars. On the contrary, in the metal-poor ($-2.0 <$ [Fe/H] < -1.0) and very metal-poor ($-3.0 <$ [Fe/H] < -2.0) regimes, the Zn and Cu lines are still well visible, but there is still a paucity of investigations.

We selected a sample of evolved stars expected to be around -2.0 in metallicity in order to investigate Cu and Zn, and we here present the results.

2 TARGET SELECTION AND OBSERVATIONS

2.1 Target selection

The stars have been selected from the Pristine photometry (see Starkenburg et al. 2017) combined with the *Gaia* EDR3 data (Gaia Collaboration 2021), as described in Bonifacio et al. (2019). Metal-poor stars from this catalogue shall be observed by WEAVE (Dalton et al. 2020) as discussed in Aguado et al. (2019). We selected metal-poor giant stars with $9.5 < G < 11$, as these stars are too bright to be observed by WEAVE.

We first selected stars bright enough to be observed with SOPHIE at the 1.93-m telescope at the Observatoire de Haute-Provence (OHP) and with a photometric metallicity around -2.0, to be observable at the end of September 2021 from OHP. We were then limited in the stellar coordinates by selecting a sample of stars to be observed in a 4-d run. For this reason, we selected also stars expected to be slightly more metal-rich.

We then selected a sample of stars to be observed with Neo-Narval at the 2-m Télescope Bernard Lyot located at the Pic du Midi at 2878-m above sea level. The observations were carried out in service mode and the fact that we had no restriction on right ascension allowed us to select the best candidate, and for this reason no metal-rich star was detected in the sample.

2.2 Observations

27 stars were observed by L. Lombardo with SOPHIE at OHP (Bouchy & Sophie Team 2006) between 2021 September 20 and 23. We used the HR mode that provides a resolving power $R =$ 75 000 and covers the spectral range 387.2–694.4 nm. The log of their observations is listed in Table 1. In Fig. 1, an observed spectrum is shown. Of the 27 observed objects, we retained 20 stars. Of the other observed stars: one object (TYC 1770−1337−1) is a

Table 1. Radial velocities and details on the observations.

Star	RA [deg]	Dec. [deg]	V_{rad} [km s^{-1}]	Date	UT	Instrument	V_{rad} *Gaia* [km s^{-1}]
1745739764412146816[a]	321.88919123759	11.24673772381	42.6283 ± 0.0025	2021-09-23	21:39:27.592	SOPHIE	43.19 ± 0.24
HU Peg	359.84236527518	13.78653405450	−177.0939 ± 0.0027	2021-09-23	00:48:20.326	SOPHIE	− 177.35 ± 0.33
TYC 1118−595−1	320.67053605163	13.26123250708	−297.3112 ± 0.0027	2021-09-20	19:27:24.679	SOPHIE	− 295.69 ± 0.44
TYC 1118−595−1	320.67053605163	13.26123250708	−297.3114 ± 0.0027	2021-09-20	20:30:08.420	SOPHIE	− 295.69 ± 0.44
TYC 1118−595−1	320.67053605163	13.26123250708	−297.2833 ± 0.0024	2021-09-21	20:43:15.166	SOPHIE	− 295.69 ± 0.44
TYC 1118−595−1	320.67053605163	13.26123250708	−297.2972 ± 0.0023	2021-09-21	21:48:13.585	SOPHIE	− 295.69 ± 0.44
TYC 1123−1454−1	321.98461188234	11.11580205916	−161.0842 ± 0.0022	2021-09-22	20:41:05.090	SOPHIE	− 159.36 ± 0.40
TYC 1125−548−1	325.93469148805	10.884461291	−96.4728 ± 0.0027	2021-09-23	22:41:52.341	SOPHIE	− 96.30 ± 0.46
TYC 1159−895−1	343.41019128982	13.80142336401	−247.1121 ± 0.0020	2021-09-24	00:45:57.893	SOPHIE	− 245.28 ± 0.23
TYC 1172−486−1	352.71221897294	10.22994243585	−164.6068 ± 0.0028	2021-09-22	23:46:31.901	SOPHIE	− 164.07 ± 0.35
TYC 1194−507−1	11.36015858646	20.18865874663	−220.6973 ± 0.0015	2021-09-24	02:49:36.069	SOPHIE	− 220.62 ± 0.14
TYC 1205−397−1	25.60006949474	16.20842014543	−215.1774 ± 0.0025	2021-09-21	02:46:03.552	SOPHIE	− 211.65 ± 1.53
TYC 1688−640−1	330.87576156536	19.44485391121	−129.9363 ± 0.0024	2021-09-23	23:44:01.623	SOPHIE	− 129.92 ± 0.44
TYC 1709−674−1	340.0191775293	21.36955712544	−119.0488 ± 0.0027	2021-09-21	22:50:45.205	SOPHIE	− 116.05 ± 0.39
TYC 1709−674−1	340.0191775293	21.36955712544	−118.9278 ± 0.0027	2021-09-22	21:43:06.711	SOPHIE	− 116.05 ± 0.39
TYC 1709−674−1	340.0191775293	21.36955712544	−118.9815 ± 0.0028	2021-09-22	22:44:35.726	SOPHIE	− 116.05 ± 0.39
TYC 1742−324−1	12.17520695121	25.8632098167	−144.9814 ± 0.0014	2021-09-23	01:50:12.156	SOPHIE	− 145.27 ± 0.32
TYC 1753−1167−1	18.76817037252	28.41816179373	−64.7050 ± 0.0020	2021-09-23	02:52:01.855	SOPHIE	− 64.78 ± 0.25
TYC 1760−612−1	29.75439204397	26.64150070754	−40.7388 ± 0.0019	2021-09-21	03:48:40.271	SOPHIE	− 53.94 ± 3.31
TYC 2086−422−1	260.1635473089	28.17628090437	−119.1516 ± 0.0019	2021-09-21	19:40:09.796	SOPHIE	− 119.27 ± 0.37
TYC 2086−422−1	260.1635473089	28.17628090437	−119.0257 ± 0.0019	2021-09-23	20:36:55.738	SOPHIE	− 119.27 ± 0.37
TYC 2207−992−1	330.64318457557	25.23600250867	−249.9804 ± 0.0021	2021-09-20	21:33:44.932	SOPHIE	− 250.15 ± 0.18
TYC 2270−1021−1	8.06790877154	34.37544943326	−48.9931 ± 0.0017	2021-09-21	01:43:48.239	SOPHIE	− 50.93 ± 0.25
TYC 2299−342−1	19.39556032887	35.10894563703	4.1301 ± 0.0013	2021-09-22	00:55:08.090	SOPHIE	− 0.32 ± 1.19
TYC 2772−378−1	359.24602579191	32.26115537377	−245.3013 ± 0.0017	2021-09-21	23:53:12.644	SOPHIE	− 244.94 ± 0.18
TYC 3084−1083−1	255.56155650328	43.47158629928	−218.6399 ± 0.0020	2021-09-22	19:37:54.825	SOPHIE	− 218.33 ± 0.32
TYC 3084−1083−1	255.56155650328	43.47158629928	−218.5810 ± 0.0020	2021-09-23	19:35:14.983	SOPHIE	− 218.33 ± 0.32
TYC 3060−408−1	238.06063090409	44.21095353327	−107.00 ± 0.08			Neo-Narval	− 107.25 ± 0.18
TYC 2457−2294−1	112.57364405527	32.94891041111	−212.73 ± 0.08			Neo-Narval	− 213.10 ± 0.25
TYC 3006−1127−1	153.06268163918	44.16492084722	126.83 ± 0.09			Neo-Narval	126.28 ± 0.24
TYC 286−299−1	180.77301654219	6.38273783758	188.19 ± 0.14			Neo-Narval	188.38 ± 0.19
TYC 1406−971−1	143.23536461939	18.38596473122	153.74 ± 0.12			Neo-Narval	153.08 ± 0.20
TYC 284−358−1	182.67671784716	3.05459391526	60.18 ± 0.07			Neo-Narval	60.01 ± 0.30
TYC 4182−1043−1	235.15863333571	61.95951610665	−99.22 ± 0.08			Neo-Narval	− 99.43 ± 0.14
TYC 3458−980−1	189.59408656055	49.61650555607	−91.87 ± 0.13			Neo-Narval	− 91.51 ± 0.22
TYC 3458−611−1	187.89255539781	48.82974228654	−17.67 ± 0.08			Neo-Narval	− 17.57 ± 0.15
TYC 891−750−1	200.01448759931	7.70738827868	88.74 ± 0.08			Neo-Narval	89.05 ± 0.31
TYC 312−1416−1	207.62957843038	3.95407002247	4.34 ± 0.07			Neo-Narval	4.28 ± 0.24
TYC 914−128−1	221.91296639868	12.39335297616	−73.81 ± 0.08			Neo-Narval	− 74.21 ± 0.36
TYC 333−942−1	223.86857608899	6.74545326013	−64.92 ± 0.36			Neo-Narval	− 64.57 ± 0.68
TYC 877−422−1	186.53618052056	10.25013586841	339.61 ± 0.13			Neo-Narval	336.97 ± 0.71
TYC 905−551−1	212.3784102112	12.06841728236	−223.33 ± 0.12			Neo-Narval	− 223.29 ± 0.28
1180300688463921792[a]	223.83323169277	10.66753837455	74.31 ± 0.38			Neo-Narval	73.75 ± 0.43

[a] *Gaia* DR3

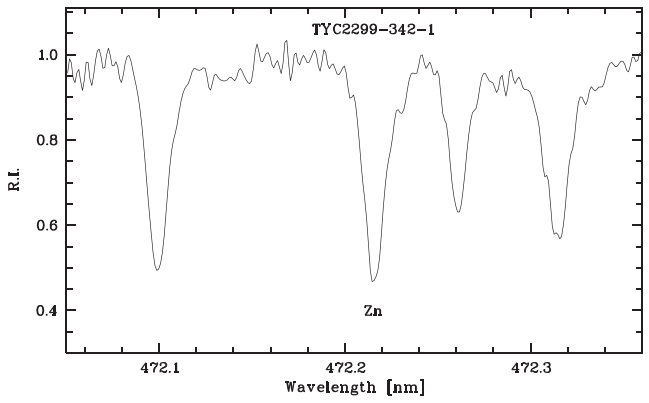

Figure 1. The spectrum of TYC 2299−342−1 in the range of a Zn I line. The S/N per pixel in this range is 47.

double lined binary system and the other six stars are too metal-rich ([Fe/H] > −0.5) for the goal of this investigation.

The radial velocities provided in Table 1 were derived by the SOPHIE pipeline using a cross-correlation with a K0 mask. We have four stars with more than one SOPHIE spectrum, and the rms of the observations is of the order of a few 10 m s^{-1}. This is larger than the errors of the individual spectra, as provided by the pipeline. It could plausibly be due to radial velocity jitter and pulsations (see e.g. Carney et al. 2003).

There are six stars (TYC 1159−895−1, TYC 1709−674−1, TYC 1760−612−1, TYC 2270−1021−1, TYC 2299−342−1, TYC 877−422−1) that are likely radial velocity variables, since the *Gaia* radial velocity differs by over 2.5σ from our measured radial velocities. The radial velocity we derived for TYC 1205−397−1 was in perfect agreement with the one derived by *Gaia* DR2 (V_{rad} = −215.12 ± 0.76 km s^{-1}) but with the new determination

by *Gaia* DR3 a difference of $-3.5\,\mathrm{km\,s^{-1}}$ appeared, which is still consistent at 2.5σ due to a larger uncertainty in the *Gaia* DR3 catalogue (see Table 1). These stars showing a difference in radial velocity between *Gaia* DR3 and SOPHIE, could be spectroscopic binaries, but we cannot detect any secondary spectrum, hence they should be SB1. We assume the veiling from a possible unseen companion to be negligible for our abundance analysis.

16 stars have been observed with Neo-Narval at the Télescope Bernard-Lyot (TBL). We used Neo-Narval with a fibre that provides a resolving power $R = 65\,000$ and covers the spectral range 370–1000 nm. The observations were acquired in service mode from 2021 September to 2022 March. For the Neo-Narval spectra, to derive the radial velocities, we shifted the spectra according to the value provided by *Gaia* DR3. The spectrum was then analysed with MyGIsFOS (see Section 4), and we used the shift determined for each line kept for the chemical analysis to correct the *Gaia* DR3 radial velocity. We do not provide a date for these measures, since the chemical analysis and the determination of radial velocity were done on the co-added spectra. Individual spectra were corrected for the barycentric velocity before co-addition. Compared to the *Gaia* DR3 radial velocities, they differ within 2.5σ; also TYC 877−422−1, whose difference in radial velocity of more than $2\,\mathrm{km\,s^{-1}}$, is anyway within the uncertainties.

Neo-Narval is a refurbishment of Narval, very recently made available to the community, so the spectra still show the need for further work on the data reduction software. To check the quality of the spectra, we investigated the chemical pattern of a standard radial-velocity star, HD 185144, to assure the quality of the observations. We selected 70 high S/N spectra observed by SOPHIE and 70 observed by Neo-Narval. We compared the abundances derived from MyGIsFOS by keeping the same stellar parameters ($T_{\rm eff} = 5338$ K, $\log\ g = 4.57$, and $\xi = 0.94\mathrm{km\,s^{-1}}$) for all the spectra. We removed three spectra from the Neo-Narval sample because the iron abundance derived was lower (by more than 0.05 dex and in one case by 0.78 dex) than A(Fe) derived from the average of the others and from the SOPHIE spectra. The elements for which we derived agreement (within 0.05 dex) from the two spectrographs are: Fe I, Na I, Al I, Si I, Ca I, Sc II, V I, Mn I, Ni I, Cu I, Zn I, Y II. We would like to stress that also the S/N in the Neo-Narval spectra is generally much lower than in the SOPHIE spectra, providing a lower set of 'good' lines to investigate.

3 KINEMATICS

The orbital parameters were computed following the same recipe as in Kordopatis et al. (2022, see section 3.1), i.e. adopting the Stäckel fudge method (Binney 2012; Sanders & Binney 2016) with the McMillan (2017) axisymmetric potential for the Galaxy and the GALPY (Bovy 2015) code. The Sun's position is assumed to be (R, Z) = (8.249, 0.0208) kpc (Bennett & Bovy 2019; Gravity Collaboration 2020), and its peculiar velocities (VR, Vϕ, VZ) = $(-9.5, 250.7, 8.56)\,\mathrm{km\,s^{-1}}$ (Gravity Collaboration 2020; Reid & Brunthaler 2020).

In Fig. 2, the angular momentum versus the square root of the radial action is shown for both the SOPHIE and Neo-Narval samples. As Galactic comparison we show the sample of SDSS Turn-Off stars from Bonifacio et al. (2021). To fix the ideas we have coloured in pink the region where the Gaia–Sausage–Enceladus (GSE) stars are expected to be found, according to Feuillet et al. (2020) ($-500\,\mathrm{kpc\,km\,s^{-1}} < L_z < 500\,\mathrm{kpc\,km\,s^{-1}}$ and $30\,(\mathrm{kpc\,km\,s^{-1}})^{1/2} < \sqrt{J_r} < 50\,(\mathrm{kpc\,km\,s^{-1}})^{1/2}$), in green what we

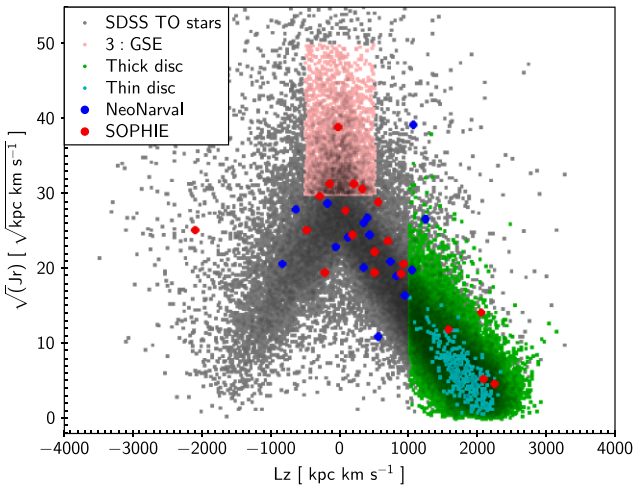

Figure 2. The SOPHIE (red dots) and the Neo-Narval (blue dots) stars compared to SDSS TO stars from Bonifacio et al. (2021) in the angular momentum–radial action plane. See text for details.

associate with the Galactic disc (thick + thin) ($L_z < 1000\,\mathrm{kpc\,km\,s^{-1}}$ and $z_{\rm max} < 3.0$ kpc) and in light blue the thin disc ($L_z < 1000\,\mathrm{kpc\,km\,s^{-1}}$ and $z_{\rm max} < 0.3$ kpc). From the orbital parameters, there are some interesting objects. 27 stars have a pericentre below 3.5 kpc from the Galactic centre, and are on high eccentricity orbits ($e > 0.5$). There is a clear anticorrelation between pericentre and eccentricity, which is obviously an observational bias. Six stars belong to the Galactic disc, three of which to the thin disc. Two of the thin disc stars are metal-poor: TYC 2270−1021−1 ([Fe/H] = −1.28) and *Gaia* DR3 1745739764412146816 ([Fe/H] = −2.05); one is slightly metal-poor TYC 22299−342−1 ([Fe/H] = −0.59). All three stars have low eccentricities, the largest being that of *Gaia* DR3 1745739764412146816 ($e = 0.33$). Four of the stars are likely members of the GSE structure (Belokurov et al. 2018; Haywood et al. 2018; Helmi et al. 2018). They span the metallicity range −1.3 to −2.4, thus in the range where most of the GSE stars are expected to fall according to the GSE metallicity distribution function (MDF) of Bonifacio et al. (2021). However, according to the GSE MDFs of Feuillet et al. (2020) and Naidu et al. (2020) such stars should be rare. All the GSE stars are α enhanced, which is expected at these metallicities, while at higher metallicities the GSE should be characterized by lower α-to-iron ratios. Thus, at these metallicities it is impossible to distinguish between GSE stars born in the accreted galaxy and those that were born in the Milky Way disc and then scattered to these low angular-momentum, high radial action orbits, by the collision. Our sample is selected purely on a chemical basis and, based on our rough orbital selections, we have 11 per cent of GSE stars and 17 per cent of disc stars (8 per cent thin disc). The small size of the sample prevents us from drawing strong conclusions from these numbers.

4 ANALYSIS

In Fig. 3, the photometric metallicity, [M/H], used to select the stars, is compared to the iron abundance, [Fe/H], derived by analysing the spectra with MyGIsFOS(Sbordone et al. 2014), keeping the same stellar parameters derived by the calibration and a micro-turbulence of $2\,\mathrm{km\,s^{-1}}$.

We find a difference of $\langle[\mathrm{Fe/H}] - [\mathrm{M/H}]\rangle = 0.22 \pm 0.31$. The agreement is very good for the 20 stars observed with SOPHIE

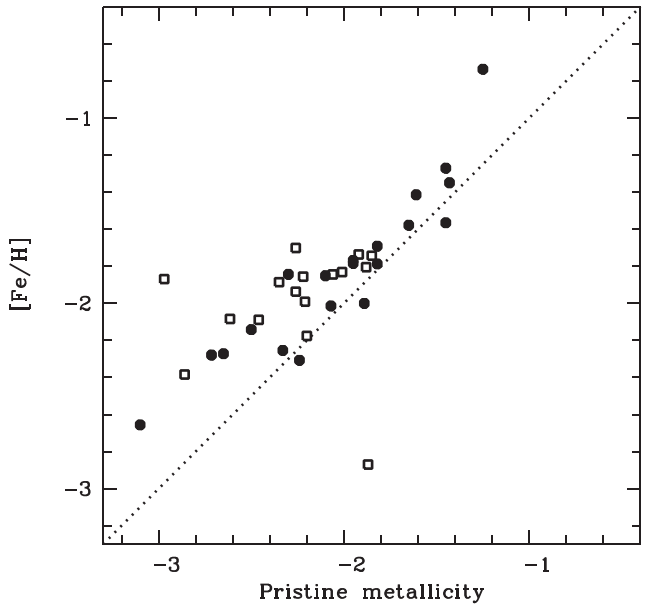

Figure 3. Comparison of the metallicity derived from the calibration and [Fe/H] derived by using $T_{\rm eff}$ and log g from the calibration. Black filled circles are the SOPHIE observations and black open squares the Neo-Narval ones.

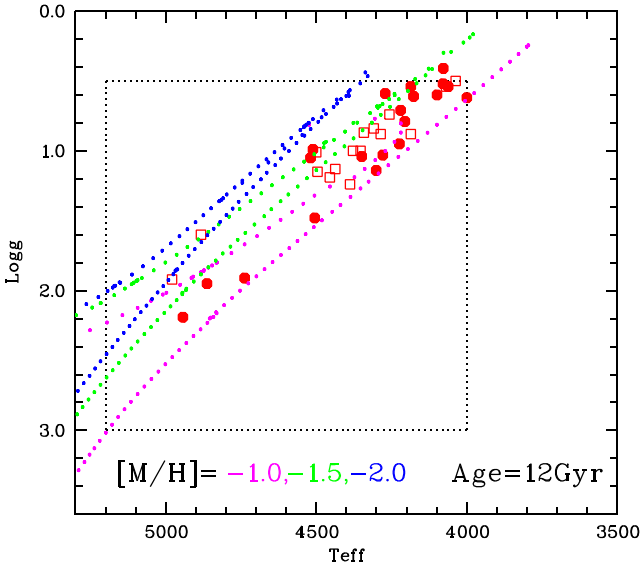

Figure 4. log g versus $T_{\rm eff}$ for the stars (red filled circles SOPHIE and red open squares Neo-Narval) compared to PARSEC isochrones (Bressan et al. 2012; Marigo et al. 2017). The black dotted lines denote the limits of the grid interpolated by MyGIsFOS.

and chemically analysed, with a maximum difference of 0.51 dex in the case of TYC 2299−342−1. In the Neo-Narval sample we have no mistake in the metal-poor selection, with a success rate of 100 per cent, but for two stars the metallicity derived from the photometry differs by about 1 dex with [Fe/H] derived from the spectra: *Gaia* DR3 1180300688463921792 has a [Fe/H] that is 1 dex lower than expected from the photometry and this could be also related to the low S/N of the spectrum; on the contrary, TYC 877−422−1 was expected to be close to −3.0 in metallicity but it is slightly more metal-rich than −2.0 in [Fe/H].

We are extremely satisfied on the success in the selection on metal-poor stars and on the general good agreement in the two metallicities. However, in the selection of the SOPHIE stars, we picked also wrong targets. In the SOPHIE sample, six stars happen to be too metal-rich for our investigation, so we consider 77 per cent the success rate on our selection. In this computation, we removed the binary star observed several nights with SOPHIE.

4.1 Stellar parameters

The adopted stellar parameters are then derived by comparing the *Gaia* DR3 data (parallax, G magnitude, BP − RP colour) to theoretical values, as described in Lombardo et al. (2021). The parallax was corrected for the zero-point (Lindegren et al. 2021).

The reddening was adopted from the Schlegel, Finkbeiner & Davis (1998) maps corrected as in Bonifacio, Monai & Beers (2000). The micro-turbulence was derived from the Mashonkina et al. (2017a) calibration. We use MyGIsFOS to derive the detailed abundances for all stars except for TYC 2270−1021−1 for which we adopt a $T_{\rm eff}$ of 4000 K instead of 3872 K as derived from the procedure, because we had no grid available for MyGIsFOS at this low temperature. The star HU Peg extrapolates in the grid for log g by less than 0.1 dex. The stars TYC877−422−1 and *Gaia* DR3 1180300688463921792 also extrapolate in log g by 0.15 dex. In Fig. 4, the adopted stellar parameters are compared to PARSEC isochrones (Bressan et al. 2012; Marigo et al. 2017). The adopted stellar parameters are reported in Table 2.

The comparison of the stellar parameters as derived from the calibration of Pristine photometry and those derived only from *Gaia* parallaxes and photometry, plus spectra, are shown in Fig. 5. One can see from the figure that the surface gravity is practically the same, while for the effective temperature the average difference is −65 ± 62 K for the SOPHIE sample and −52 ± 38 K for the Neo-Narval, being usually cooler the adopted $T_{\rm eff}$, with the largest difference being −141 K. Mucciarelli, Bellazzini & Massari (2021) derive a colour–temperature relation combining the InfraRed Flux Method (IRFM) from González Hernández & Bonifacio (2009) with the photometry from *Gaia* EDR3. When we compare the adopted effective temperatures to the values derived by using the calibration by Mucciarelli et al. (2021), we find an average difference of $T_{\rm adopted} - T_{\rm Mucciarelli} = -51 \pm 52$ K and of log $g_{\rm adopted}$ − log $g_{\rm Mucciarelli} = 0.02 \pm 0.02$ for the SOPHIE sample and −46 ± 48 and −0.01 ± 0.02 for the Neo-Narval stars. We assumed as uncertainty for the effective temperature 100 K.

We compared the adopted $T_{\rm eff}$ also to the effective temperatures derived from the González Hernández & Bonifacio (2009) calibration. Being a bright sample of stars, we retrieved the 2MASS and V Johnson photometry in the AAVSO Photometric All-Sky Survey APASS (Henden et al. 2012) and the JHKs magnitudes in the infrared bands from the Two Micron All-Sky Survey (2MASS; Skrutskie et al. 2006). The colours were de-reddened using the maps from Schlegel et al. (1998). For a few stars, with uncertainties higher than 0.1 mag, the SDSS (York et al. 2000) g and r magnitudes, of the SDSS Photometric Catalogue, Release 12 (Alam et al. 2015), have been converted into Johnson V. Removing the stars TYC 2270−1021−1 and *Gaia* DR3 1180300688463921792, with a V APASS photometry inconsistent with *Gaia* DR3, we derived a good agreement with the adopted $T_{\rm eff}$: $T_{\rm adopted} - T_{\rm IRFM} = -9 \pm 83$ K.

For the surface gravity, the largest effect is the uncertainty on the parallax. When adding/subtracting the uncertainty on the parallax when deriving log g we derive a difference of 0.05. We assumed 0.1 dex as uncertainty in log g.

Table 2. The adopted stellar parameters.

Star	$T_{\rm eff}$ [K]	log g [gcs]	ξ km s^{-1}	[Fe1/H] dex	S/N @480 nm
1745739764412146816	4349	1.04	1.94	−2.05	23
HU Peg	4078	0.41	2.12	−2.21	26
TYC 1118−595−1	4186	0.54	2.11	−2.12	40
TYC 1123−1454−1	4177	0.61	2.09	−2.43	34
TYC 1125−548−1	4519	1.05	2.05	−2.41	25
TYC 1159−895−1	4206	0.79	1.98	−1.97	38
TYC 1172−486−1	4863	1.95	1.81	−2.52	33
TYC 1194−507−1	4224	0.95	1.87	−1.34	36
TYC 1205−397−1	4279	1.03	1.94	−2.41	26
TYC 1688−640−1	4738	1.91	1.71	−1.73	27
TYC 1709−674−1	4271	0.59	2.15	−2.46	43
TYC 1742−324−1	4099	0.60	2.01	−1.84	53
TYC 1753−1167−1	4301	1.14	1.84	−1.58	32
TYC 1760−612−1	4511	0.99	2.00	−1.53	37
TYC 2086−422−1	4062	0.54	2.04	−1.96	33
TYC 2207−992−1	4220	0.71	2.02	−1.79	30
TYC 2270−1021−1	4000	0.62	2.00	−1.28	30
TYC 2299−342−1	4943	2.19	1.58	−0.59	52
TYC 2772−378−1	4505	1.48	1.78	−1.58	44
TYC 3084−1083−1	4079	0.52	2.04	−1.82	42
TYC 3060−408−1	4266	0.70	2.05	−1.92	9
TYC 2457−2294−1	4374	0.90	2.04	−2.22	13
TYC 3006−1127−1	4365	0.75	2.03	−2.17	9
TYC 286−299−1	4888	1.52	1.98	−2.04	10
TYC 1406−971−1	4982	1.87	1.86	−2.00	11
TYC 284−358−1	4305	0.80	2.03	−1.98	12
TYC 4182−1043−1	4384	0.97	1.97	−1.88	7
TYC 3458−980−1	4447	1.06	1.97	−1.92	6
TYC 3458−611−1	4462	1.14	1.93	−1.85	11
TYC 891−750−1	4400	1.16	1.90	−1.86	10
TYC 312−1416−1	4335	0.70	2.05	−1.79	13
TYC 914−128−1	4208	0.77	1.98	−1.76	8
TYC 333−942−1	4517	0.88	2.18	−2.59	3
TYC 877−422−1	4076	0.35	2.12	−1.96	6
TYC 905−551−1	4483	1.05	1.99	−1.76	6
1180300688463921792	4076	0.35	2.12	−3.03	3

For micro-turbulence, the values derived from the equivalent width – abundance balance show an average difference with the adopted one of about 0.2 km s^{-1}. We assumed this value of 0.2 km s^{-1} as the uncertainty in the micro-turbulence.

The LAMOST spectra of 13 stars in the sample are investigated by Zhang, Liu & Deng (2020) by using a machine learning method. The average difference in metallicity we find is of −0.27, with the largest of −1.36 dex for *Gaia* DR3 1180300688463921792. Removing this star, the difference in metallicity becomes −0.18 dex. This small but systematic difference is surely related to the hotter (by −154 K on average) $T_{\rm eff}$ adopted by Zhang et al. (2020).

The same uncertainties we applied for similar quality data by Matas Pinto et al. (2022). The uncertainties in the stellar parameters imply uncertainties in the derived abundances. These uncertainties are largely discussed by Matas Pinto et al. (2022). In Table 3, we report an average uncertainty in the abundances related to the uncertainties in the stellar parameters.

4.2 Chemical investigation

The abundances have been derived with MyGIsFOS (see Sbordone et al. 2014). The adopted solar values are from Caffau et al. (2011) and Lodders, Palme & Gail (2009) and are listed in Table 4. The abundances are provided in two online tables (one for the SOPHIE sample and one for the Neo-Narval sample) with the line-to-line scatter as uncertainties as discussed in the appendix (see Section A). In Appendix B, an explanation on the lines used for the chemical investigation is provided for a table deposited to the Centre de Données astronomiques de Strasbourg (CDS).

For several elements (Na, Mg, Al, Si, Ca, Ti, Fe, Zn, and Zr), we computed a line-by-line investigation on the departure from NLTE. The NLTE calculations were performed using the methods treated by Alexeeva, Pakhomov & Mashonkina (2014, Na I), Mashonkina (2013, Mg I), Mashonkina, Belyaev & Shi (2016a, Al I), Mashonkina (2020, Si I), Mashonkina, Sitnova & Belyaev (2017b, Ca I), Sitnova, Mashonkina & Ryabchikova (2016, Ti II), Mashonkina et al. (2011, Fe I-Fe II), Sitnova et al. (2022, Zn I), and Velichko, Mashonkina &

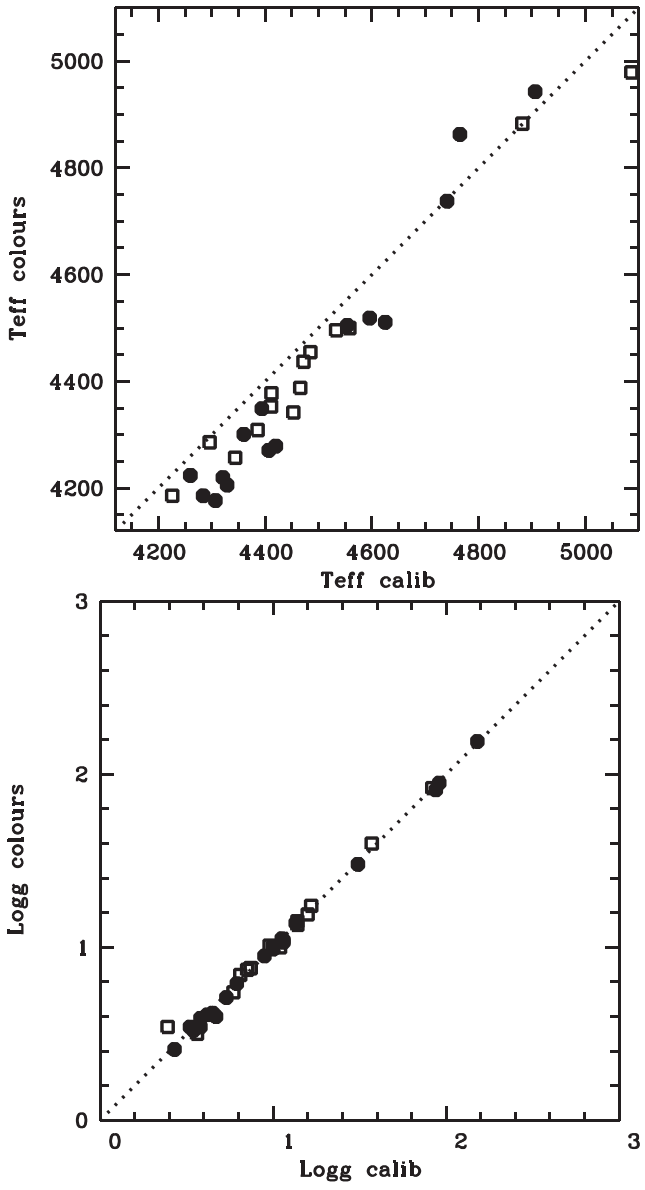

Figure 5. Comparison of the effective temperature and surface gravity when derived from the *Gaia* EDR3 data combined with Pristine narrow band photometry (horizontal axis) compared to *Gaia* DR3 and spectroscopic metallicities (vertical axis). Black filled circles represent the SOPHIE observations and open squares the Neo-Narval.

Table 3. Sensitivity of abundances on atmospheric parameters.

Element	$\Delta T_{\rm eff}$ 100 K	$\Delta \log g$ 0.2 dex	$\Delta\xi$ 0.2 km s^{-1}
Na I	0.08	0.02	0.01
Mg I	0.08	0.03	0.03
Al I	0.06	0.01	0.00
Si I	0.03	0.02	0.01
Ca I	0.10	0.02	0.04
Sc I	0.17	0.01	0.00
Sc II	0.02	0.11	0.04
Ti I	0.16	0.02	0.03
Ti II	0.01	0.08	0.06
V I	0.18	0.01	0.00
Cr I	0.14	0.02	0.03
Cr II	0.04	0.08	0.01
Mn I	0.14	0.02	0.01
Fe I	0.12	0.01	0.05
Fe II	0.08	0.11	0.05
Co I	0.14	0.01	0.00
Ni I	0.10	0.01	0.02
Cu I	0.13	0.01	0.00
Zn I	0.04	0.06	0.03
Zr I	0.15	0.01	0.00
Zr II	0.02	0.10	0.04
Ba II	0.05	0.10	0.20

Table 4. The adopted solar abundances and the sensitivity of abundances on atmospheric parameters.

Element	A(X)$_\odot$	Δ
Na I	6.30	0.08
Mg I	7.54	0.10
Al I	6.47	0.07
Si I	7.52	0.04
Ca I	6.33	0.11
Sc II	3.10	0.13
Ti I	4.90	0.17
Ti II	4.90	0.11
V I	4.00	0.18
Cr I	5.64	0.15
Cr II	5.64	0.09
Mn I	5.37	0.14
Fe I	7.52	0.13
Fe II	7.52	0.13
Co I	4.92	0.14
Ni I	6.23	0.10
Cu I	4.21	0.13
Zn I	4.62	0.09
Y II	2.21	0.10
Zr I	2.62	0.13
Zr II	2.62	0.11
Ba II	2.17	0.23

Nilsson (2010, Zr II). We applied the code DETAIL (Giddings 1981; Butler 1984) with a modified opacity package (as described by Mashonkina et al. 2011). The NLTE abundance corrections, $\Delta_{\rm NLTE} = \varepsilon_{\rm NLTE} - \varepsilon_{\rm LTE}$, for individual spectral lines were computed with the code LINEC (Sakhibullin 1983) that uses the LTE and NLTE level populations from DETAIL.

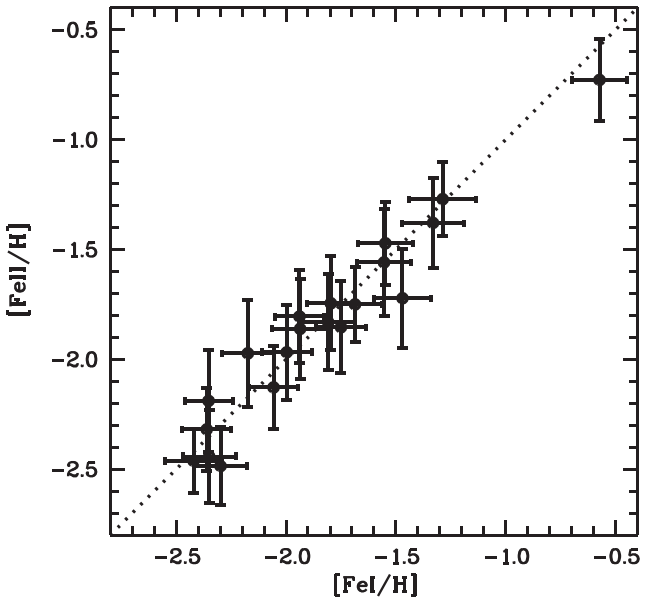

Figure 6. [FeI/H] versus [FeII/H]. In the case of Fe I, NLTE corrections are included. The error bars are the line-to-line scatter.

4.2.1 Iron

For the SOPHIE sample, several Fe I features (from 148 to 235) have been investigated to derive the iron abundance from neutral lines and for the stars in the sample we derived $-2.51 < [\rm Fe/H] < -0.58$. The line-to-line scatter is generally small ($\langle\sigma\rangle = 0.12 \pm 0.01$ dex) with 0.15 dex as the highest value in the case of TYC 2270−1021−1. For a subsample of Fe I lines, we computed the NLTE correction to be applied to the LTE abundance. To verify that the NLTE correction is not strongly influenced by our choice of lines, we derived the LTE iron abundance only from the Fe I lines selected to compute the NLTE correction and compared it to the Fe abundance derived from the complete sample of Fe I lines. We derived an extremely good agreement in the LTE iron abundance, with a difference on average close to zero and, in any case, within 0.03 dex.

We investigated from 15 to 25 features to derive the Fe abundance from Fe II lines and we derived $-2.49 < [\rm Fe/H] < -0.73$. The line-to-line scatter (from 0.15 to 0.24 dex) in the sample was $\langle\sigma\rangle = 0.20 \pm 0.03$, larger than that for neutral Fe lines. The NLTE corrections for Fe II are negligible, being the largest of only −0.01 dex for the lines at 492.392 and 501.843 nm. We can then safely use the LTE investigation for the Fe abundance derived from Fe II lines.

The iron abundance derived from neutral and ionized lines are generally in good agreement, and anyway always within the uncertainties. In Fig. 6, we show the iron abundance derived from Fe II lines compared to the one from Fe I lines, taking into account the NLTE corrections in the latter case.

The spectra observed with Neo-Narval have lower S/N ratios than the SOPHIE sample, with an average value of 28 at 600 nm and a minimum of 9, to be compared to an average of 53 and a minimum of 38 for the SOPHIE sample. This translate in a smaller number of Fe I lines used (from 70 to 136 except for the two spectra of lowest S/N). The Neo-Narval sample spans in metallicity: $-2.59 < [\rm Fe/H] < -1.75$. One star stands out from the range with [Fe/H] = −3.03, but the quality of the spectrum is poor, with S/N = 9 at 600 nm. Also the spectrum of TYC 333−942−1 has a similar S/N ratio, and only 16 Fe I lines are kept in the investigation. No Fe II line was retained in the analysis of the Neo-Narval spectra.

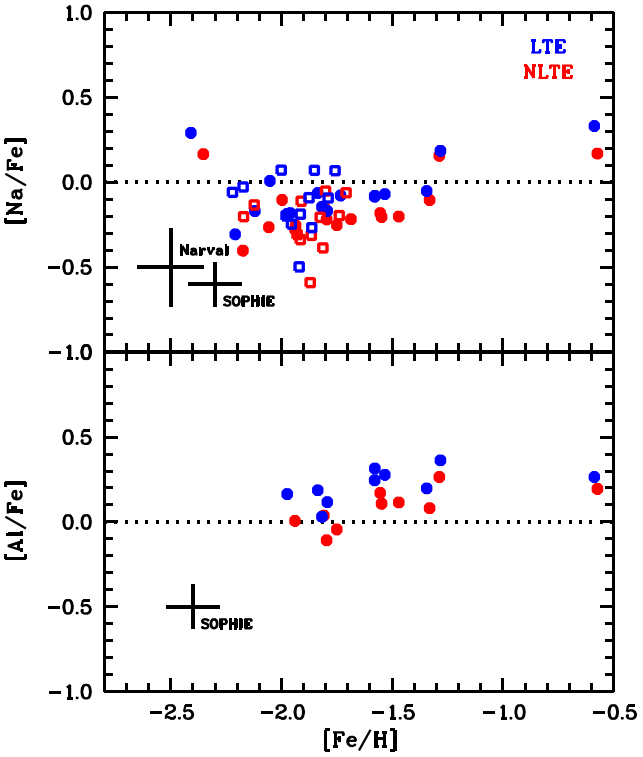

Figure 7. [Na/Fe] and [Al/Fe] versus [Fe/H], LTE in blue and NLTE in red. For Na, filled circles are the SOPHIE stars and open squares the Neo-Narval ones. Error bars are average values based on the line-to-line scatter.

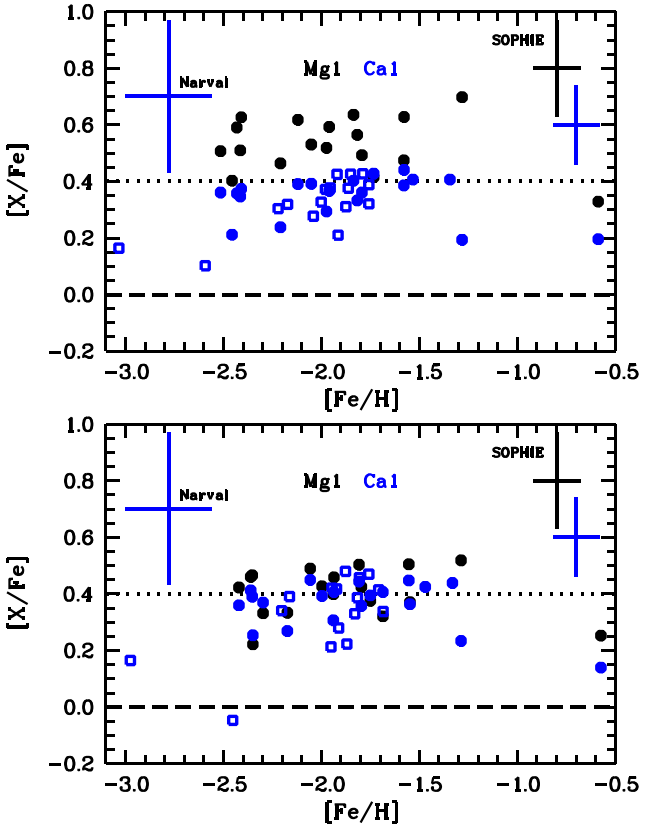

Figure 8. [Mg/Fe] (black symbols) and [Ca/Fe] (blue symbols) versus [Fe/H]. In the upper panel, the LTE results are presented and in the lower panel the NLTE corrections are applied. Filled circles are the SOPHIE stars, open squares the Neo-Narval ones. No Mg abundance has been derived in the Neo-Narval sample. Error bars are average values based on the line-to-line scatter.

4.2.2 Sodium

Sodium has been derived in 16 SOPHIE and in 12 Neo-Narval stars, by using up to four of the lines at: 498.281, 568.263, 568.820, and 616.074 nm. We investigated the NLTE effects for individual lines, finding the NLTE corrections for the stars in the range from −0.15 to −0.03 dex. The results are shown in Fig. 7.

4.2.3 Aluminuim

For 10 stars in the SOPHIE sample, we could derive the Al abundance by using from one to three Al I lines (555.706, 669.602, and 669.618 nm), deriving for the sample $\langle$[Al/Fe]$\rangle = 0.22 \pm 0.10$. The NLTE corrections are non-negligible, in the range from −0.12 to −0.06. In Fig. 7, the results are shown.

4.2.4 Magnesium

Only for 18 stars in the SOPHIE sample, we could derive Mg abundance with $\langle$[Mg/Fe]$\rangle = 0.53 \pm 0.10$. From one to four lines have been used for the abundance determination (457.109, 470.299, 552.840, and 571.108 nm), but for the majority of cases (12 stars on 18) the Mg abundance is based on one single line, the one at 571.1 nm.

We investigated the NLTE effects on the Mg I lines and obtained that for all but one star for which the Mg abundance is based on more than one line, the line-to-line scatter on [Mg/H] is drastically reduced when the NLTE correction is applied (the only exception being TYC 1172−486−1). NLTE corrections for the forbidden line at 457.109 nm are positive, for the other three lines they are negative, with only the exception for the line at 470.299 nm for the star TYC 1172−486−1. The NLTE correction ranges from −0.18 to +0.01.

In Fig. 8 [Mg/Fe] versus [Fe/H] is shown (together with the [Ca/Fe] rations), the LTE investigation and after the application of the NLTE corrections. From the figure, it is well visible that after applying the NLTE correction the [Mg/Fe] star-to-star scatter decreases and it is also clear that while in LTE [Mg/Fe] are systematically larger than [Ca/Fe], in NLTE the two α elements behave, as expected, very consistently.

We provide no Mg abundance for the Neo-Narval sample (see Section 2.2).

4.2.5 Silicon

A sample of Si I lines (from one to 15) allowed us to derive Si abundance for 18 stars in the SOPHIE sample. For the sample, we obtained: $\langle$[Si/Fe]$\rangle = 0.43 \pm 0.14$, with, as expected, the lowest value for the most metal-rich star (TYC 2299−342−1: [Si/Fe]=0.18). The highest [Si/Fe] value (HU Peg: [Si/Fe] = 0.78) is based on just one Si I line, and the other two stars with a relatively high [Si/Fe] (TYC 1123−1454−1: [Si/Fe] = 0.62 ± 0.18 on three lines; TYC 1205−397−1: [Si/Fe] = 0.67 ± 0.21 on six lines) have the highest line-to-line scatter in the sample.

In the Neo-Narval sample, we could derive Si abundance for 12 stars by analysing from one to 11 lines. The $\langle$[Si/Fe]$\rangle = 0.48 \pm 0.14$ is consistent with the SOPHIE sample. Two stars show a high [Si/Fe]

ratio: TYC 2457−2294−1 with [Si/Fe] = 0.79 based on five lines and TYC 286−299−1 with [Si/Fe] = 0.79 based on one line.

4.2.6 Calcium

For all the stars in the SOPHIE sample we could derive the Ca abundance, by using from 13 to 25 lines. We derived a mean LTE abundance of: $\langle$Ca/Fe$\rangle = 0.34 \pm 0.08$ with a small line-to-line scatter (from 0.05 to 0.12 dex). Having a substantial sample of lines for the Ca investigation, we decided to exclude the Ca I lines: at 452.692 nm, because its upper level is not included in the model atom, and at 657.277 nm, because for this forbidden line the NLTE computations are not completely reliable. Without these two lines, we could base our investigation on a sample of 11 to 23 lines and derive an A(Ca) that is extremely close to what obtained without excluding these lines. The average line-to-line scatter improves, from 0.070 to 0.067 dex. The NLTE corrections range from −0.04 to +0.15.

For all the stars in the Neo-Narval sample, we could derive the Ca abundance by investigating from 4 to 18 lines and deriving $\langle$Ca/Fe$\rangle = 0.32 \pm 0.09$, very consistent with the SOPHIE sample. With [Ca/Fe] < 0.2, two stars (TYC 333−942−1 and *Gaia* DR3 1180300688463921792) are slightly poor in Ca, but the abundance determination is based on only four lines.

In Fig. 8, the [Ca/Fe] ratios (in LTE and NLTE) versus [Fe/H] are shown together with the [Mg/Fe] ratios.

4.2.7 Titanium

For all the stars in the SOPHIE sample, we could derive the Ti abundance from both Ti I and Ti II lines.

To derive A(Ti) from Ti II lines, we used from 14 to 26 features. For the sample we obtained $\langle$[Ti/Fe]$\rangle = 0.38 \pm 0.11$ when Fe abundance is from Fe II lines. The line-to-line scatter in the A(Ti) determination is $\langle\sigma\rangle = 0.13 \pm 0.04$. The NLTE corrections for A(Ti) when derived from Ti II lines are small (never exceeding 0.03 dex in absolute value). We can then safely use the LTE investigation.

Titanium abundance from Ti I is very sensitive to NLTE effects (see Mashonkina, Sitnova & Pakhomov 2016b), we then decided to rely on the Ti II results for A(Ti).

4.2.8 Scandium

One Sc I line at 568.6 nm was used to derive Sc abundance for 10 stars in the SOPHIE sample, obtaining for the sample $\langle$[Sc/Fe]$\rangle = 0.12 \pm 0.08$. Nine stars of the 10 have an oversolar [Sc/Fe] ratio.

For all the stars in the sample A(Sc) was derived from a set of Sc II lines (from one to seven) and we obtained $\langle$[Sc/Fe]$\rangle = 0.30 \pm 0.11$, with Fe abundance from Fe II lines in this case. The [Sc/Fe] ratio is rather large, and this oversolar value is not justified by a large line-to-line scatter, that for Sc II is $\langle\sigma\rangle = 0.14 \pm 0.05$.

Sc I lines yield the lower [Sc/Fe] ratios compared with those from the Sc II lines and this is due to the use of the LTE assumption. As shown by Zhang, Gehren & Zhao (2008), Sc I is subject to overionization in the solar atmosphere resulting in weakened lines and positive NLTE abundance corrections. For the Sc I at 568.6 nm, Zhang et al. (2008) computed $\Delta_{\rm NLTE} = 0.14$ dex. As a rule, the departures from LTE grow towards lower surface gravity and lower metallicity. Therefore, $\Delta_{\rm NLTE}$ for the 568.6 nm Sc I in our sample stars is expected to be positive and greater than 0.1 dex. Sc II is a majority species in the atmospheres of our sample stars, and the departures from LTE for Sc II lines are expected to be smaller. Using the model atom of Sc II from Mashonkina & Romanovskaya (2022), we computed the NLTE abundance corrections for the Sc II lines investigated for all the stars and we verified that the NLTE corrections are small, with an average $|\Delta_{\rm NLTE}| < 0.07$ dex for all stars.

4.2.9 Vanadium

From a sample of V I lines (from one to 19), we derived V abundances for all the SOPHIE stars in the sample. The [V/Fe] ratio is close to solar for all ($\langle$[V/Fe]$\rangle = 0.04 \pm 0.16$) but one star (TYC 1172−486−1, [V/Fe] = +0.60 from one line). When removing this star for the sample, we derive: $\langle$[V/Fe]$\rangle = 0.01 \pm 0.09$ and the number of V I lines used is from four to 19.

4.2.10 Chromium

We investigated a sample of Cr I (from 8 to 19) and of Cr II (from 3 to 7) lines to derive the Cr abundances for all the SOPHIE stars. The average [Cr/Fe] ratios are close to zero for both ionization ($\langle$[Cr/Fe]$\rangle$ of -0.08 ± 0.07 for neutral and 0.04 ± 0.09 for ionized Cr).

4.2.11 Manganese

A sample from two to 20 lines allowed us to derive Mn abundance for all the stars in the SOPHIE sample. The [Mn/Fe] ratio is negative for all the stars ($\langle$[Mn/Fe]$\rangle = -0.28 \pm 0.07$). We could derive Mn abundance for 12 stars in the Neo-Narval sample using from one to eight Mn lines, with results in perfect agreement with the SOPHIE sample ($\langle$[Mn/Fe]$\rangle = -0.29 \pm 0.14$).

These undersolar ratios are compatible with the literature values and are due to strong NLTE effects (see Bergemann & Gehren 2008). Matas Pinto et al. (2022) investigated two stars of similar parameters and searched for the NLTE corrections computed by Bergemann & Gehren (2008), deriving an NLTE effect larger than +0.3 dex. With such a correction, the [Mn/Fe] ratio of our stars would become around zero.

Looking at the results by Bergemann & Gehren (2008) for some of the lines we used, we have in fact an average NLTE correction of 0.40 dex, with the smallest values unsurprisingly for TYC 2299−342−1, which is the more metal-rich star in the sample, and the highest of about 0.5 dex for the most metal-poor stars (TYC 1125−548−1, TYC 1172−486−1, and TYC 1205−397−1).

4.2.12 Cobalt

For 19 stars of the SOPHIE sample, we could derive A(Co) by using a sample from three to 17 Co I lines. For the sample we derived $\langle$[Co/Fe]$\rangle = 0.11 \pm 0.06$, slightly oversolar, but, taking into account the uncertainties ($\langle\sigma\rangle = 0.13 \pm 0.04$), compatible with zero. An NLTE correction for these stars derived by Bergemann, Pickering & Gehren (2010) would be in the range +0.3 to +0.4 dex, bringing the [Co/Fe] ratios oversolar. According to Bergemann et al. (2010), taking into account the lines we used with available NLTE corrections, for our stars the corrections are in the range +0.16 to +0.64 with +0.38 as the average value.

4.2.13 Nickel

All the SOPHIE stellar spectra have a good sample of Ni I lines (from 17 to 57) that allowed us to derive A(Ni). For all the stars in the sample the [Ni/Fe] ratio is close to zero ($\langle$[Ni/Fe]$\rangle = -0.02 \pm 0.05$).

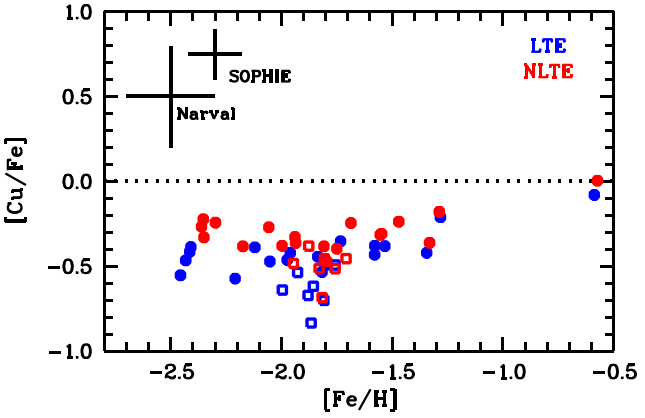

Figure 9. [Cu/Fe] versus [Fe/H], filled circles the SOPHIE sample and open squares the Neo-Narval. The uncertainties represent the average line-to-line scatter, except for Cu in the Neo-Narval stars, where it is derived from the Cayrel formula added in quadrature with the line-to-line scatter in Fe.

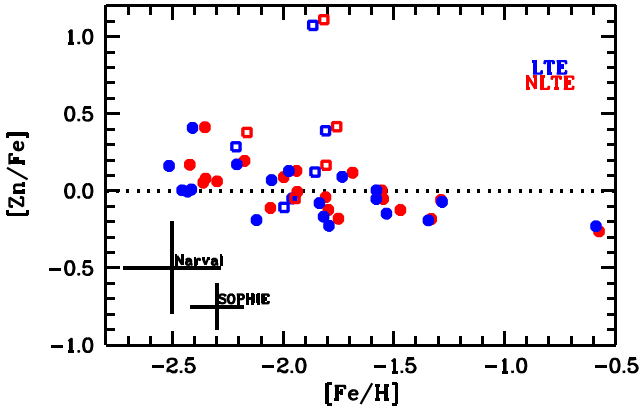

Figure 10. [Zn/Fe] versus [Fe/H], filled circles the SOPHIE stars and open squares the Neo-Narval ones. The uncertainties are derived as for Cu.

In the Neo-Narval sample, we derived Ni abundance for 14 stars, with $\langle$[Ni/Fe]$\rangle = -0.03 \pm 0.08$, perfectly consistent with the SOPHIE sample.

4.2.14 Copper

The Cu investigation is based on four Cu I lines at 510.5, 521.8, 570.0, and 578.2 nm. For all the stars except one in the SOPHIE sample, we could derive the Cu abundance using from one to four lines. For the sample, we derived: $\langle$[Cu/Fe]$\rangle = -0.41 \pm 0.11$, a very small star-to-star scatter, which reduces even more, to 0.08, if we remove the most metal-rich star (TYC 2299−342−1, with [Cu/Fe] = −0.08). If we remove also the next most Cu-rich star (TYC 2270−1021−1, with [Cu/Fe] = −0.21), we obtain a star-to-star scatter of 0.06. Only in seven stars in the Neo-Narval sample could we derive the Cu abundance using the 578.2 nm line and, for two stars, also the line at 570.0 nm, providing $\langle$[Cu/Fe]$\rangle = -0.62 \pm 0.11$. In Fig. 9, the results are shown.

The underabundance of Cu with respect to Fe of all the stars investigated is surely related to NLTE effects on Cu. In fact, Cu I is subject to overionisation in the range of stellar parameters of the stars here investigated. For the stars whose A(Cu) is based on more than one line, the line-to-line scatter is small (in the range 0.03 to 0.12 dex). The 510.5, 570.0, and 578.2 nm lines belong to the same multiplet, so we expect not too different NLTE corrections for these three lines. The 521.8 nm line arises from the higher excitation level ($E_{\rm exc}$ = 3.82 eV) compared with that of the first three lines ($E_{\rm exc}$ = 1.39–1.64 eV). For dwarf stars with [Fe/H] $\simeq -1.5$, Yan et al. (2016) obtain slightly smaller NLTE corrections for 521.8 nm compared with that for 510.5 nm. Thus, we do not expect an increase in the line-to-line scatter in NLTE.

Shi et al. (2018) investigated the NLTE effects on the 510.5 nm Cu I line for two metal-poor set of parameters ($T_{\rm eff}$/log g/[Fe/H] of 4600/1.60/−2.50 and 4600/1.32/−2.63, respectively) and derived NLTE–LTE of +0.30 and +0.40 dex, respectively. Our stars bracket in parameters the cases investigated by Shi et al. (2018), we can then expect NLTE corrections of this order of magnitude.

From the same 510.5 nm Cu I line, Andrievsky et al. (2018) derived an NLTE correction of about +0.3 dex for HD 9051 (4925/1.95/−1.78) and about +0.7 dex for HD 122563 (4600/1.10/−2.82). The larger NLTE correction by Andrievsky et al. (2018) with respect to Shi et al. (2018) could be due to a smaller log g and/or smaller [Fe/H] of the stars by Andrievsky et al. (2018), or some differences in the Cu model atom.

To make our own mind on the NLTE effects on the Cu I lines, we produced a new model atom of Cu I–Cu II (Sitnova, in preparation) to take into account the NLTE corrections. The model includes 59 levels of Cu I, 20 levels of Cu II, and the ground state of Cu III. The list of energy levels and transitions is taken from R. Kurucz webpage.[1] For the majority of levels, the fine structure is taken into account. The high-excitation levels of Cu I are combined in four super-levels according to their parity. For Cu I, we use photoionization cross-sections from Liu et al. (2014) calculated with the R-matrix method. For Cu II, we calculate hydrogen-like cross-sections. We employ data for inelastic collisions with hydrogen atoms from Belyaev, Yakovleva & Kraemer (2021). Electron-impact excitation rates are calculated with the van Regemorter (1962) and Woolley & Allen (1948) formulae, for radiatively allowed and forbidden transitions, respectively. Electron impact ionization is calculated with the Seaton (1962) formula. Using new data for Cu + H collisions leads to smaller non-LTE corrections.

As it can be appreciated from the figure, the NLTE corrections result in a smaller star-to-star scatter at any metallicity. The general trend at low metallicities is still flat, like in LTE, but the mean value is slightly higher by about 0.1 dex.

4.2.15 Zinc

For all stars in the SOPHIE sample we could derive A(Zn) by using from one to two Zn I lines (472.215 and 481.052 nm). For the sample we derive: $\langle$Zn/Fe$\rangle = -0.02 \pm 0.16$. For six of the Neo-Narval stars, we could derive A(Zn), with $\langle$Zn/Fe$\rangle = 0.19 \pm 0.47$.

The NLTE correction is not negligible and ranges from −0.02 to + 0.18. In Fig. 10, the effects of NLTE are shown by comparing the LTE and NLTE results.

One of the stars observed with Neo-Narval, TYC 891-750-1, displays a very high [Zn/Fe] ∼1.1. This value is even higher than the two Zn-rich stars highlighted by Lombardo et al. (2022): HE 2252-4335 and CS 30312-100. Unfortunately, we do not have an Ni measurement for this star. Lombardo et al. (2022) highlighted the existence of two branches in the [Ni/Fe] – [Zn/Fe] plane (see fig. 8 of Lombardo et al. 2022). One branch with high [Zn/Fe] that Lombardo et al. (2022) suggested as formed from gas polluted by hypernovae

[1] http://kurucz.harvard.edu/atoms.html

(see e.g. Nomoto, Kobayashi & Tominaga 2013) and a branch with lower [Zn/Fe] that they suggested as formed from gas polluted by normal supernovae.

4.2.16 Yttrium

The Y abundances have been derived from 7 to 12 Y II lines in all the stars in the SOPHIE sample. For the stellar sample, we derived $\langle$[Y/Fe]$\rangle = -0.14 \pm 0.12$.

4.2.17 Zirconium

For 12 stars in the SOPHIE sample, we could derive A(Zr) from one Zr I line at 473.948 nm. For the 12 stars we derived: $\langle$[Zr/Fe]$\rangle = -0.03 \pm 0.21$. The NLTE correction is positive and large, ranging from +0.39 to +0.77.

One to two Zr II lines (at 461.394 and 511.227 nm) allowed us to derive A(Zr) for 16 stars in the Neo-Narval sample, that provides $\langle$[Zr/Fe]$\rangle = 0.62 \pm 0.24$. Taking into account the NLTE corrections, this provides $\langle$Zr/Fe$\rangle = 0.55 \pm 0.21$.

5 DISCUSSION

For all the investigated elements, except marginally Sc II, the abundances derived for these stars are compatible with the literature samples of stars with comparable parameters that we looked at (Fulbright 2000; Gratton et al. 2000; Ishigaki, Chiba & Aoki 2012; Ishigaki, Aoki & Chiba 2013) (see Appendix C).

The stars are classical metal-poor stars, enhanced in α elements. One star, TYC 1172−486−1, stands out for the high [V/Fe] $= 0.60 \pm 0.19$ ratio. The star TYC 1205−397−1 has the largest [Zn/Fe] and [Zr/Fe] ratios in the sample ([Zn/Fe] $= +0.41 \pm 0.11$ and [Zr/Fe] $= +0.50 \pm 0.15$). In the Neo-Narval sample, two stars (TYC 333−942−1 and *Gaia* DR3 1180300688463921792) seem low in Ca, but both stars have poor-quality spectra. One star in the Neo-Narval sample, TYC 891−750−1, shows a high [Zn/Fe] ratio ([Zn/Fe] $= 1.05 \pm 0.25$), while TYC 914−128−1 shows the lowest [Zn/Fe] ratio ([Zn/Fe] $= -0.31 \pm 0.26$).

We selected the 19 SOPHIE stars more metal-poor than [Fe/H] < -1.0 and we investigated the star-to-star scatter of the element-to-iron ratios. We found that they are generally well below 0.10 dex (0.07 dex for Ca and Cr II, 0.08 dex for Mg, 0.10 dex for Ti II, 0.04 dex for Ni, 0.06 dex for Co and Cr I). For Zn instead the star-to-star scatter is 0.16 dex. Even removing the 'high Zn' star TYC 1205−397−1 the star to star scatter remains larger than for the other elements (0.12 dex). The mean error on Zn is 0.07 dex, thus this extra scatter cannot be due to larger errors on the Zn abundances. To further investigate the scatter in Zn we divided the sample into two subsamples: $-2 \leq$ [Fe/H] < -1 (11 stars) and [Fe/H] < -2 (8 stars). In this case, the star-to-star scatter is 0.11 and 0.17 dex, respectively. If we exclude from the most metal-poor sample TYC 1205-397-1 (7 stars), the stars-to-star scatter is 0.12 dex. An increase in the scatter of Zn, with respect to other elements, could be explained if a fraction of our stars were low-mass long-lived stars formed in an environment predominantly enriched by a PISN (>50 per cent of the total amounts of metals), but also by subsequent generation of 'normal' Pop II SNe (Salvadori et al. 2019). In fig. 7 of Salvadori et al. (2019, right-hand panel), when normal SNII contribute to pollute the ISM at a 50 per cent level, there is a double peak in the zinc-to-iron value, the highest being at [Zn/Fe]≈ -0.3. In Fig. 11, we have assembled some literature values for [Zn/Fe], the extremely low [Zn/Fe] of BD+80 245, LAMOSTJ112456.61+453531.3 and TYC 4267−2023−1 clearly stand out. It is interesting to concentrate on the stars in our sample around [Zn/Fe] $= -0.3$: as discussed above, they are consistent with being formed from $\leq$50 per cent of PISN and the rest of SNII polluted gas.

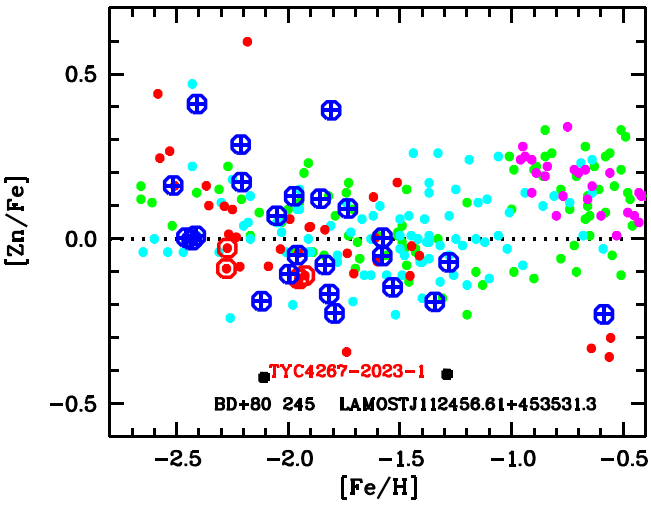

Figure 11. [Zn/Fe] versus [Fe/H]: from this analysis (blue crossed circles); the MINCE project (Cescutti et al. 2022, red filled circles and the two stars with two independent spectra are surrounded by an open red circle); from Mishenina et al. (2002, green circles); from Mishenina et al. (2011, pink circles); from Ishigaki et al. (2013, light blue circles); the Zn-poor stars BD+80 245 by Ivans et al. (2003) and LAMOSTJ112456.61+453531.3 by Xing et al. (2019) (black squares).

The fact that there is a continuity in the [Zn/Fe] ratio, from solar to about −0.4, could be related to the fraction of the PISN contribution to the gas from where the star formed. This is not obviously the case for Cu whose star-to-star scatter (0.08 dex) is similar to the values derived for the other elements. But the relatively high star-to-star scatter for Zn could be simply related to the fact that there is a known correlation [Zn/Fe] versus [Fe/H] (99 per cent confidence for the SOPHIE sample) and this dependence increases the star-to-star scatter. This was pointed out in other samples of metal-poor stars (see e.g. Lombardo et al. 2022).

The likely PISN descendent BD+80 245 (see Fig. 11), analysed by Ivans et al. (2003, $T_{\rm eff}$/log g of 5225/3.0) and Roederer et al. (2014, 5360/3.15), has been already discussed by Salvadori et al. (2019). We investigated in our sample if we could find other stars likely descendent from PISN, by comparing the observed stellar chemical pattern with those theoretically derived by Salvadori et al. (2019) for a gaseous environment predominantly enriched by PISNe (>50 per cent of metals in the gas). The χ^2 methodology is described in section 5.2 from Salvadori et al. (2019) and it will be further detailed in Aguado et al. (in preparation). In brief: we built a grid of theoretical predictions from Salvadori et al. (2019) including mass of Pop III, percentage of Pop III, and $f*/f_{\rm dil}$ (with $f*$ the star formation efficiency and $f_{\rm dil}$ the effectively fraction of metals injected into the interstellar medium and of the gas used to dilute them (see Salvadori et al. 2019, for details) as free parameters. Then we use the FERRE code to interpolate between the nodes of the grid, calculate the best set of PISN parameters, and provide the best model (a set of elemental abundances from C to Zn) according to these parameters.

In our sample, three candidates (the Halo TYC 1118−595−1, the two GSE TYC 1194−507−1, and TYC 2207−992−1) seem to be

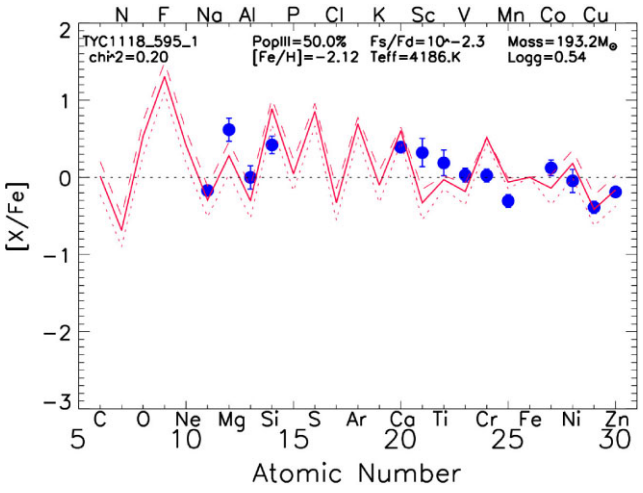

Figure 12. Comparison of the chemical abundances derived for TYC 1118−595−1 (blue dots) compared to the PISN model best fit (red line) with the following parameters $f_{\rm PISN} = 50$ per cent; $f_*/f_{\rm dil} = 10^{-2.3}$; and $m_{\rm PISN} = 193.2\,{\rm M}_\odot$. For reference, we also show a model with same parameters but higher PISN contribution $f_{\rm PISN} = 65$ per cent (red dotted line) and with different PISN mass $m_{\rm PISN} = 208\,{\rm M}_\odot$. Main stellar parameters are also shown.

interesting. When compared to the theoretical models the stars are compatible as being formed from:

(i) TYC 1118−595−1 a gas enriched 50 per cent by a PISN of initial mass of almost 200 $\rm M_\odot$, with a high probability ($\chi^2_{\rm PISN} = 0.20$, see Fig. 12);
(ii) TYC 2207−992−1 a gas mostly (83 per cent) enriched by an almost 170 $\rm M_\odot$, with a quite high probability ($\chi^2_{\rm PISN} = 0.38$);
(iii) TYC 1194−507−1 also a gas mostly (90 per cent) enriched by an almost 170 $\rm M_\odot$, but with a lower probability ($\chi^2_{\rm PISN} = 0.50$) than the previous star.

Here, $\chi^2_{\rm PISN} = \chi^2/(N - M)$ where N is the number of fitted abundances and M is the number of free parameters in the model. Unfortunately, we could not get any information on nitrogen abundance because in the range of the CN band (at about 388 nm) the S/N was really low. Anyway, all these stars are mixed, and part of carbon has been converted into nitrogen. We stress that we do not claim that these chemical patterns can only be formed if the original gas is partially polluted by PISNs. There may be other, probably more contrived ways, to explain them. What is important is that we have employed the full chemical pattern of these stars and did not rely uniquely on few elements (Aguado et al., in preparation). This sample is certainly very small, but it is remarkable that we have found three stars that could have been formed by PISN polluted material. Once a much larger sample of Zn abundances in metal-poor stars shall be available, for example from the 4MOST Milky Way Halo High-Resolution Survey (Christlieb et al. 2019), the fraction of these possible PISN descendants will strongly constrain the number of PISNs that polluted the early Galaxy.

In Fig. 12, we show the observed and best-fitting abundance pattern for TYC 1118−595−1. For the lighter elements, we clearly see an odd-even effect, as expected from the PISN nucleosynthesis as well as for the Ni-Cu-Zn sequence. We attribute deviations from a strict odd-even effect to the fact that we are not seeing 'pure' PISN ejecta, but material that has also been mixed with SNII polluted material, thus weakening the odd-even effect. An odd-even effect at this level is also predicted by some core-collapse SNe models (e.g. Tominaga, Umeda & Nomoto 2007), thus the detected odd-even effect, by itself, cannot discriminate between diluted PISN ejecta and core-collapse SNe ejecta.

A complete and systematic investigation on the probability and characteristic on the stellar formation from a gas enriched by a PISN is presented by Aguado et al. (in preparation).

6 CONCLUSIONS

The Pristine photometry, coupled with *Gaia* parallaxes and photometry, proved to be extremely effective in selecting stars of metallicity around −2.0 (77 per cent success for the SOPHIE sample and 100 per cent success for the Neo-Narval sample).

This outstanding efficiency in selecting metal-poor stars allowed us to investigate a sample of 36 bright giant stars for which we derived detailed chemical abundances using small-size telescopes. The main goal of this investigation was to increase the statistics of Cu and Zn measurements in this poorly examined metallicity regime to look for possible PISN descendants. The frequency of stars like BD+80 245 (Salvadori et al. 2019), will provide us information on the high-mass end of the primordial initial mass function ($140\,{\rm M}_\odot < M_{\rm PopIII} < 260\,{\rm M}_\odot$), which is populated by the stellar progenitors of energetic PISNe. Three stars in the sample (TYC 1118−595−1, TYC 2207−992−1, and TYC 1194−507−1) are possible PISN descendants. Clearly the number of stars investigated in the present paper is too small to derive conclusions. The WEAVE (Dalton et al. 2020) survey at high resolution could provide a large sample of Cu and Zn measurements in metal-poor stars. If the green grating, covering the wavelength range 473 nm to 545 nm, is used, we will be able to measure the Zn I 481.0 nm and the Cu I 510.5 nm lines for all the metal-poor Pristine targets, which shall be available to WEAVE.

The kinematics of our sample confirms the existence of metal-poor star on disc orbits (17 per cent of the sample), and even on thin disc orbits (8 per cent of the sample). Four stars belong to the GSE structure, one more (TYC 11159−895−1, [Fe/H] = –1.97) is on the border. Given the variety of ways in which the GSE structure has been defined in different kinematical spaces, in the literature we may consider also this star a likely member of GSE. So in a chemically selected sample, spanning the metallicity range $-2.6 \leq$ [Fe/H] ≤ -1.3 we have from 11 to 14 per cent of stars belonging to GSE and 17 per cent belonging to the disc (thin and thick). This leaves us with about 70 per cent of the stars that are something else, likely: stars formed in the disc and scattered into halo orbits; stars that were formed in other galaxies or stellar clusters and accreted by the Milky Way; and, possibly, stars formed '*in situ*' in the Milky Way Halo. To determine if any fraction of the Halo was indeed formed '*in situ*', it is very important to understand the formation of the Milky Way. To form stars '*in situ*', the Halo must have had a gas component, with overdensities large enough to start the star formation process at least in some places. At present we cannot confirm, nor refute the existence of this '*in situ*' component. Again, the WEAVE–Pristine sample shall provide a large sample of stars to study correlations between kinematical and chemical properties, from which the present results on the fractions of metal-poor stars belonging to the different Galactic components shall be more robustly confirmed, or refuted.

ACKNOWLEDGEMENTS

We are grateful to Arturo Lopez Ariste and Philippe Mathias of the Observatoire Midi Pyrénées for their help in dealing with the Neo-Narval data and for the great improvements in the Neo-Narval DRS

and for reprocessing all the spectra with the improved version. We are grateful to the CNRS Institut National des Sciences de l'Univers - Programme National de Cosmologie et Galaxies for allocating to our project time on the 1.93-m telescope at Observatoire de Haute Provence and on the 2-m Télélescope Bernard Lyot at the Observatoire du Pic du Midi. We gratefully acknowledge support from the French National Research Agency (ANR) funded project 'Pristine' (ANR-18-CE31-0017). SS and AD acknowledge funding from the European Research Council (ERC) under the European Union's Horizon 2020 research and innovation programme (grant agreement no. 804240). JIGH acknowledges financial support from the Spanish Ministry of Science and Innovation (MICINN) project PID2020-117493GB-I00. TS acknowledges support from the MK project, grant 5127.2022.1.2. EFA acknowledge support from the Agencia Estatal de Investigación del Ministerio de Ciencia e Innovación (AEI-MCINN) under grant 'At the forefront of Galactic Archaeology: evolution of the luminous and dark matter components of the Milky Way and Local Group dwarf galaxies in the *Gaia* era' with reference PID2020-118778GB-I00/10.13039/501100011033. EFA also acknowledges support from the 'María Zambrano' fellowship from the Universidad de La Laguna. This work presents results from the European Space Agency (ESA) space mission *Gaia*. *Gaia* data are being processed by the *Gaia* Data Processing and Analysis Consortium (DPAC). Funding for the DPAC is provided by national institutions, in particular the institutions participating in the Gaia MultiLateral Agreement (MLA). The *Gaia* mission website is https://www.cosmos.esa.int/gaia. The *Gaia* archive website is https://archives.esac.esa.int/gaia.

This is based on observation obtained at Observatoire de Haute-Provence in programme 21B.PNGC.MATA and at Observatoire du Pic de Midi under programme L212N07.

DATA AVAILABILITY

The abundances derived in the present analysis are provided in machine readable format at the Centre de Données astronomiques de Strasbourg. The SOPHIE spectra are available from the SOPHIE archive http://atlas.obs-hp.fr/sophie/. The Neo-Narval archive is not yet operational, until then, the DRS reduced spectra are available on request directly from P. Bonifacio (Piercarlo.Bonifacio@observatoiredeparis.psl.eu).

REFERENCES

Aguado D. S. et al., 2019, MNRAS, 490, 2241
Alam S. et al., 2015, ApJS, 219, 12
Alexeeva S., Pakhomov Y., Mashonkina L., 2014, Astron. Lett., 40, 406
Andrievsky S., Bonifacio P., Caffau E., Korotin S., Spite M., Spite F., Sbordone L., Zhukova A. V., 2018, MNRAS, 473, 3377
Belokurov V., Erkal D., Evans N. W., Koposov S. E., Deason A. J., 2018, MNRAS, 478, 611
Belyaev A. K., Yakovleva S. A., Kraemer W. P., 2021, MNRAS, 501, 4968
Bennett M., Bovy J., 2019, MNRAS, 482, 1417
Bergemann M., Gehren T., 2008, A&A, 492, 823
Bergemann M., Pickering J. C., Gehren T., 2010, MNRAS, 401, 1334
Bihain G., Israelian G., Rebolo R., Bonifacio P., Molaro P., 2004, A&A, 423, 777
Binney J., 2012, MNRAS, 426, 1328
Bisterzo S., Gallino R., Pignatari M., Pompeia L., Cunha K., Smith V., 2004, Mem. Soc. Astron. Ital., 75, 741
Bisterzo S., Pompeia L., Gallino R., Pignatari M., Cunha K., Heger A., Smith V., 2005, Nucl. Phys. A, 758, 284
Bonifacio P., Monai S., Beers T. C., 2000, AJ, 120, 2065
Bonifacio P. et al., 2019, MNRAS, 487, 3797
Bonifacio P. et al., 2021, A&A, 651, A79
Bouchy F., Sophie Team, 2006, in Arnold L., Bouchy F., Moutou C., eds, Tenth Anniversary of 51 Peg-b: Status of and Prospects for Hot Jupiter Studies. Published by Frontier Group, Paris, p. 319
Bovy J., 2015, ApJS, 216, 29
Bressan A., Marigo P., Girardi L., Salasnich B., Dal Cero C., Rubele S., Nanni A., 2012, MNRAS, 427, 127
Butler K., 1984, PhD thesis, University of London
Caffau E., Ludwig H. G., Steffen M., Freytag B., Bonifacio P., 2011, Sol. Phys., 268, 255
Carney B. W., Latham D. W., Stefanik R. P., Laird J. B., Morse J. A., 2003, AJ, 125, 293
Cescutti G. et al., 2022, preprint (arXiv:2211.06086)
Christlieb N. et al., 2019, The Messenger, 175, 26
Dalton G. et al., 2020, in Evans C. J., Bryant J. J., Motohara K., eds, Proc. SPIE Conf. Ser. Vol. 11447, Ground-Based and Airborne Instrumentation for Astronomy VIII. SPIE, Bellingham, p. 1144714
de Bennassuti M., Salvadori S., Schneider R., Valiante R., Omukai K., 2017, MNRAS, 465, 926
Delgado Mena E., Tsantaki M., Adibekyan V. Z., Sousa S. G., Santos N. C., González Hernández J. I., Israelian G., 2017, A&A, 606, A94
Duffau S. et al., 2017, A&A, 604, A128
Feuillet D. K., Feltzing S., Sahlholdt C. L., Casagrande L., 2020, MNRAS, 497, 109
Fulbright J. P., 2000, AJ, 120, 1841
Gaia Collaboration, 2021, A&A, 649, A1
Giddings J., 1981, PhD thesis, University of London
González Hernández J. I., Bonifacio P., 2009, A&A, 497, 497
Gratton R. G., Sneden C., Carretta E., Bragaglia A., 2000, A&A, 354, 169
Gravity Collaboration, 2020, A&A, 636, L5
Haywood M., Di Matteo P., Lehnert M. D., Snaith O., Khoperskov S., Gómez A., 2018, ApJ, 863, 113
Helmi A., Babusiaux C., Koppelman H. H., Massari D., Veljanoski J., Brown A. G. A., 2018, Nature, 563, 85
Henden A. A., Levine S. E., Terrell D., Smith T. C., Welch D., 2012, J. Am. Assoc. Var. Star Obs., 40, 430
Hirai Y., Saitoh T. R., Ishimaru Y., Wanajo S., 2018, ApJ, 855, 63
Ishigaki M. N., Chiba M., Aoki W., 2012, ApJ, 753, 64
Ishigaki M. N., Aoki W., Chiba M., 2013, ApJ, 771, 67
Ivans I. I., Sneden C., James C. R., Preston G. W., Fulbright J. P., Höflich P. A., Carney B. W., Wheeler J. C., 2003, ApJ, 592, 906
Kordopatis G. et al., 2022, preprint (arXiv:2206.07937)
Kratz K. L., Farouqi K., Mashonkina L. I., Pfeiffer B., 2008, New Astron. Rev., 52, 390
Lindegren L. et al., 2021, A&A, 649, A4
Liu Y. P., Gao C., Zeng J. L., Yuan J. M., Shi J. R., 2014, ApJS, 211, 30
Lodders K., 2019, preprint (arXiv:1912.00844)
Lodders K., Palme H., Gail H. P., 2009, Landolt Börnstein, 4B, 712
Lombardo L. et al., 2021, A&A, 656, A155
Lombardo L. et al., 2022, A&A, 665, A10
McMillan P. J., 2017, MNRAS, 465, 76
Marigo P. et al., 2017, ApJ, 835, 77
Mashonkina L., 2013, A&A, 550, A28
Mashonkina L., 2020, MNRAS, 493, 6095
Mashonkina L., Romanovskaya A., 2022, Astron. Lett., 48, 577
Mashonkina L., Gehren T., Shi J.-R., Korn A. J., Grupp F., 2011, A&A, 528, A87
Mashonkina L., Belyaev A. K., Shi J.-R., 2016a, Astron. Lett., 42, 366
Mashonkina L. I., Sitnova T. N., Pakhomov Y. V., 2016b, Astron. Lett., 42, 606
Mashonkina L., Jablonka P., Pakhomov Y., Sitnova T., North P., 2017a, A&A, 604, A129
Mashonkina L., Sitnova T., Belyaev A. K., 2017b, A&A, 605, A53
Matas Pinto A. d. M. et al., 2022, Astron. Nachr., 343, e210032
Mishenina T. V., Kovtyukh V. V., Soubiran C., Travaglio C., Busso M., 2002, A&A, 396, 189

Mishenina T. V., Gorbaneva T. I., Basak N. Y., Soubiran C., Kovtyukh V. V., 2011, Astron. Rep., 55, 689
Mishenina T., Kovtyukh V., Soubiran C., Adibekyan V. Z., 2016, MNRAS, 462, 1563
Mucciarelli A., Bellazzini M., Massari D., 2021, A&A, 653, A90
Naidu R. P., Conroy C., Bonaca A., Johnson B. D., Ting Y.-S., Caldwell N., Zaritsky D., Cargile P. A., 2020, ApJ, 901, 48
Nomoto K., Kobayashi C., Tominaga N., 2013, ARA&A, 51, 457
Pignatari M., Gallino R., Heil M., Wiescher M., Käppeler F., Herwig F., Bisterzo S., 2010, ApJ, 710, 1557
Reid M. J., Brunthaler A., 2020, ApJ, 892, 39
Roederer I. U., Barklem P. S., 2018, ApJ, 857, 2
Roederer I. U., Preston G. W., Thompson I. B., Shectman S. A., Sneden C., Burley G. S., Kelson D. D., 2014, AJ, 147, 136
Romano D., Matteucci F., 2007, MNRAS, 378, L59
Romano D., Karakas A. I., Tosi M., Matteucci F., 2010, A&A, 522, A32
Rossi M., Salvadori S., Skúladóttir Á., 2021, MNRAS, 503, 6026
Sakhibullin N. A., 1983, Tr. Kazanskaia Gorodkoj Astron. Obs., 48, 9
Salvadori S., Bonifacio P., Caffau E., Korotin S., Andreevsky S., Spite M., Skúladóttir Á., 2019, MNRAS, 487, 4261
Sanders J. L., Binney J., 2016, MNRAS, 457, 2107
Sbordone L., Caffau E., Bonifacio P., Duffau S., 2014, A&A, 564, A109
Schlegel D. J., Finkbeiner D. P., Davis M., 1998, ApJ, 500, 525
Seaton M. J., 1962, in Bates D. R., ed., Atomic and Molecular Processes. Academic Press, New York, p. 375
Shi J. R., Yan H. L., Zhou Z. M., Zhao G., 2018, ApJ, 862, 71
Sitnova T. M., Mashonkina L. I., Ryabchikova T. A., 2016, MNRAS, 461, 1000
Sitnova T. M., Yakovleva S. A., Belyaev A. K., Mashonkina L. I., 2022, MNRAS, 515, 1510
Skrutskie M. F. et al., 2006, AJ, 131, 1163
Starkenburg E. et al., 2017, MNRAS, 471, 2587
Tominaga N., Umeda H., Nomoto K., 2007, ApJ, 660, 516
van Regemorter H., 1962, ApJ, 136, 906
Velichko A. B., Mashonkina L. I., Nilsson H., 2010, Astron. Lett., 36, 664
Woolley R. D. V. R., Allen C. W., 1948, MNRAS, 108, 292
Woosley S. E., Heger A., Weaver T. A., 2002, Rev. Mod. Phys., 74, 1015
Xing Q.-F., Zhao G., Aoki W., Honda S., Li H.-N., Ishigaki M. N., Matsuno T., 2019, Nat. Astron., 3, 631
Yan H. L., Shi J. R., Zhao G., 2015, ApJ, 802, 36
Yan H. L., Shi J. R., Nissen P. E., Zhao G., 2016, A&A, 585, A102
York D. G. et al., 2000, AJ, 120, 1579
Zhang H. W., Gehren T., Zhao G., 2008, A&A, 481, 489
Zhang B., Liu C., Deng L.-C., 2020, ApJS, 246, 9

APPENDIX A: ABUNDANCES

Two online tables provide the stellar parameters and the detailed chemical abundances. For each set of data a table is provided because the delivered abundances are not the same for the two sets of data.

For both samples we provide: the name of the star, the stellar parameters ($T_{\rm eff}$, log g, ξ), and for each element X: the abundance A(X), the line-to-line scatter, and the number of lines. In the case, the abundance is based on one single line, the σ provided is the highest among the other elements.

For the SOPHIE sample, the abundances provided are for: Fe (from Fe I lines), Na, Mg, Al, Si, Ca, Sc (from Sc I and Sc II lines), Ti (from Ti I and Ti II lines), V, Cr (from Cr I and Cr II lines), Mn, Fe (from Fe I and Fe II lines), Co, Ni, Cu, Zn, Sr, Y, Zr (from Zr I and Zr II lines), Ba, in this order. The abundance from Fe I lines is repeated to be close to the stellar parameters and then next to the values relative to the Fe II lines. For the Neo-Narval sample, the abundances provided are for: Fe, Na, Si, Ca, Mn, Ni, Cu, and Zn, in this order. No detection for the element X provide an empty space in the table in the column A(X), 0.000 in the line-to-line scatter and 0 for number of lines.

APPENDIX B: LINES USED FOR THE CHEMICAL INVESTIGATION

The online table available at the CDS contains, for the lines used, for each element, for each star, the oscillator strength and the lower energy (in $\rm cm^{-1}$).

APPENDIX C: PLOT WITH THE ABUNDANCES

We here provide the plots (see Figs C1 and C2) of the abundances derived, compared to the literature results. In Table C1, the Pristine names for all stars analysed are provided.

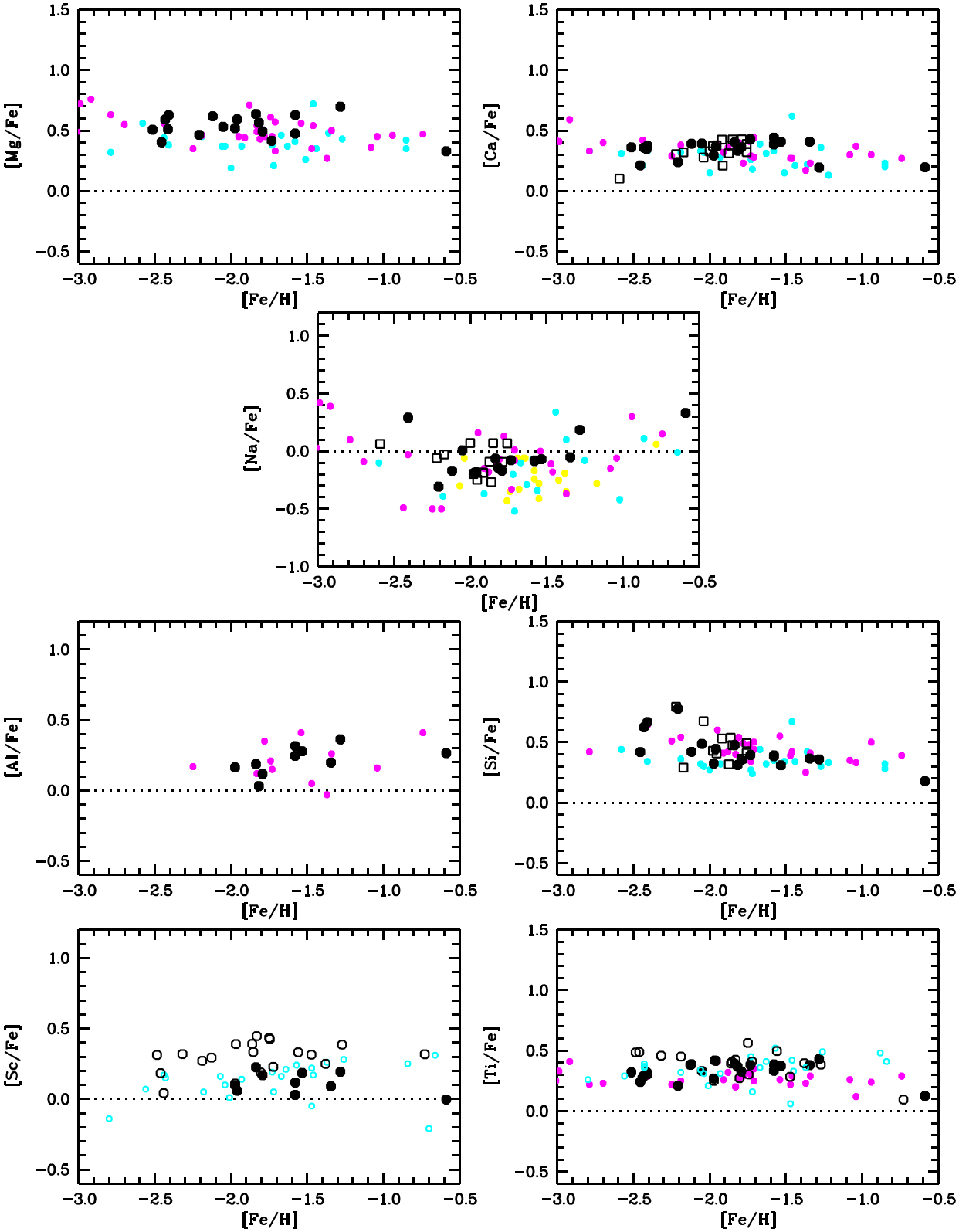

Figure C1. Abundances. Reference samples: yellow: Gratton et al. (2000); violet: Fulbright (2000); light blue: Ishigaki et al. (2012, 2013). Open symbols for the Sc and Ti panels refer to abundances from ionized Sc, Ti and Fe.

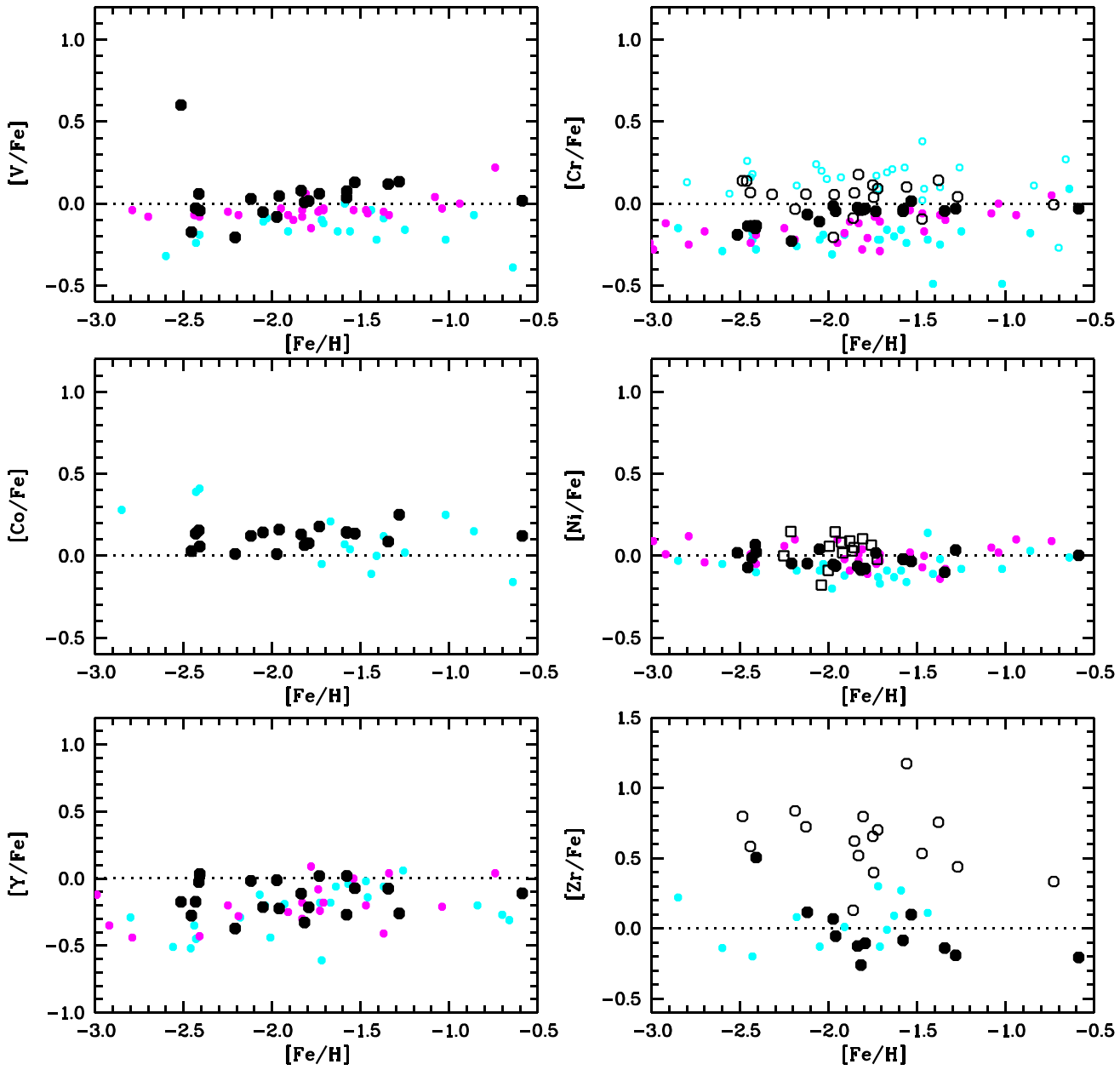

Figure C2. Abundances. Reference samples: yellow: Gratton et al. (2000); violet: Fulbright (2000); light blue: Ishigaki et al. (2012, 2013). Open symbols for the Cr and Zr panels refer to abundances from ionized Cr, Zr, and Fe.

Table C1. Identification and Pristine identification for our targets.

Main identification	Pristine identification
TYC 2270−1021−1	Pristine_008.06789207+34.37548830
TYC 1194−507−1	Pristine_011.36015797+20.18855860
TYC 1742−324−1	Pristine_012.17517471+25.86319920
TYC 1753−1167−1	Pristine_018.76822472+28.41813090
TYC 2299−342−1	Pristine_019.39557838+35.10896300
TYC 1205−397−1	Pristine_025.60008812+16.20835300
TYC 1760−612−1	Pristine_029.75453758+26.64141460
TYC 2457−2294−1	Pristine_112.57359314+32.94884110
TYC 1406−971−1	Pristine_143.23533630+18.38591960
TYC 3006−1127−1	Pristine_153.06271362+44.16487500
TYC 286−299−1	Pristine_180.77297974+06.38266660
TYC 284−358−1	Pristine_182.67672729+03.05452230
TYC 877−422−1	Pristine_186.53616333+10.25012490
TYC 3458−611−1	Pristine_187.89250183+48.82968900
TYC 3458−980−1	Pristine_189.59397888+49.61645130
TYC 891−750−1	Pristine_200.01441956+07.70733360
TYC 31−2−1416−1	Pristine_207.62947083+03.95404720
TYC 905−551−1	Pristine_212.37841797+12.06830790
TYC 914−128−1	Pristine_221.91290283+12.39337250
Gaia DR3 1180300688463921792	Pristine_223.83322144+10.66756150
TYC 333−942−1	Pristine_223.86860657+06.74538900
TYC 4182−1043−1	Pristine_235.15843201+61.95952610
TYC 3060−408−1	Pristine_238.06059265+44.21089550
TYC 3084−1083−1	Pristine_255.56152344+43.47154620
TYC 2086−422−1	Pristine_260.16348267+28.17633630
TYC 1118−595−1	Pristine_320.67050171+13.26118370
Gaia DR3 1745739764412146816	Pristine_321.88916016+11.24667260
TYC 1123−1454−1	Pristine_321.98461914+11.11573890
TYC 1125−548−1	Pristine_325.93469238+10.88442230
TYC 2207−992−1	Pristine_330.64309692+25.23588940
TYC 1688−640−1	Pristine_330.87582397+19.44488910
TYC 1709−674−1	Pristine_340.01919556+21.36958120
TYC 1159−895−1	Pristine_343.41021729+13.80131910
TYC 1172−486−1	Pristine_352.71221924+10.22986980
TYC 2772−378−1	Pristine_359.24597168+32.26105120
HU Peg	Pristine_359.84237671+13.78651710

This paper has been typeset from a TEX/LATEX file prepared by the author.